Quaternary Science Reviews 128 (2015) 81–97

Contents lists available at ScienceDirect

Quaternary Science Reviews

journal homepage: www.elsevier.com/locate/quascirev

A 37,000-year environmental magnetic record of aeolian dust deposition from Burial Lake, Arctic Alaska

J.M. Dorfman [a, *], J.S. Stoner [a], M.S. Finkenbinder [b], M.B. Abbott [b], C. Xuan [a], G. St-Onge [c]

[a] Oregon State University, College of Earth, Ocean, and Atmospheric Sciences (CEOAS), Corvallis, OR, USA
[b] University of Pittsburgh, Department of Geology and Planetary Science, Pittsburgh, PA, USA
[c] Canada Research Chair in Marine Geology, Institut des sciences de la mer de Rimouski (ISMER) & GEOTOP, Rimouski, Québec, Canada

ARTICLE INFO

Article history:
Received 6 January 2015
Received in revised form
23 June 2015
Accepted 13 August 2015
Available online xxx

Keywords:
Burial Lake
Alaska
Environmental magnetism
Paleoclimate
Dust
S-Ratios
Coercivity
Magnetite
Hematite
Deglaciation

ABSTRACT

Environmental magnetism and radiocarbon dating of Burial Lake sediments constrain the timing and magnitude of regional aeolian deposition for the Noatak region of western Arctic Alaska for the last ~37,000 years. Burial Lake (68.43°N, 159.17°W, 21.5 m water depth) is optimally located to monitor regional dust deposition because it is perched above local drainage and isolated from glacial processes. Cores collected in the summer of 2010 were studied through the application of magnetizations and progressive alternating field (AF) demagnetization of u-channel samples, with additional data provided by computed tomography (CT) derived density, hysteresis measurements, isothermal remanent magnetization (IRM) acquisition experiments, organic carbon content, biogenic silica, physical grain size, radiocarbon dating of wood, seeds, and plant macrofossils, point source magnetic susceptibility, and X-ray fluorescence (XRF). With similar magnetic properties to regional Alaskan loess deposits, low coercivity, highly magnetic material deposited during the late-Pleistocene contrasts with a high coercivity, weakly magnetic component found throughout the record, consistent with locally-derived detritus. The relative proportion of low coercivity to high coercivity magnetic material, defined by the S-Ratios, is used to reconstruct the regional input of dust to the basin over time. A four-fold decrease in the low coercivity component through the deglacial transition is interpreted to reflect diminished dust input to the region. Comparisons with potential sources of dust show that the timing of deposition in Burial Lake is largely consistent with general aridity, lack of vegetative cover, and increased windiness, rather than glacial advances or retreats. The influence from subaerial exposure of continental shelves cannot be ruled out as a significant far-field source of dust to interior Alaska during the Last Glacial Maximum (LGM), but is unlikely to have been the sole source, or to have contributed to increased dust in both the early and late Holocene.

1. Introduction

Aeolian dust has long been used as a proxy indicator for paleoclimate conditions and atmospheric transport pathways (Rea, 1994). Much focus has been given to late-Quaternary glacial-interglacial variations in “dustiness,” with increased glacial dust flux attributed to colder temperatures, increased wind intensities, source aridity, limited vegetative cover, supply of glacier-derived silt, and broad exposure of continental shelves from lowered sea level (Muhs et al., 2003a). Besides acting as an environmental tracer, aerosolic dust can also directly impact climate through radiative forcing (Tegen et al., 1996; Kohfeld and Harrison, 2001), or by fertilizing the world's oceans, thereby promoting phytoplankton blooms, which regulate atmospheric carbon dioxide (Hutchins and Bruland, 1998). At present however, the sources of dust and the forcing mechanisms responsible for its production, availability, transport, and deposition are poorly understood, thus limiting our ability to spatially reconstruct variations in dust flux, or usefully incorporate that information in general circulation models (GCMs).

In Alaska, the majority of dust-related paleoclimate data are derived from thick terrestrial loess deposits that accumulate along major river valleys and blanket large areas of the landscape (e.g., Péwé, 1955). Determining the sources and depositional history of the Alaskan loess in relation to the timing of external

* Corresponding author.
E-mail address: jdorfman@coas.oregonstate.edu (J.M. Dorfman).

http://dx.doi.org/10.1016/j.quascirev.2015.08.018
0277-3791/

environmental forcing mechanisms has been hindered by the often discontinuous and difficult to date nature of the deposits, as well as diagenetic processes that can alter the physical and chemical properties of these sediments (e.g., Liu et al., 1999). Lakes provide a low energy depositional setting, capable of producing continuous paleoclimate archives that may be less, or at least differently, influenced by the physical and chemical processes that hinder interpretation of terrestrial loess deposits. While loess deposits are entirely composed of the material of interest, complicating any flux interpretations, lake sediments contain only an admixture that allows variations in dust, timing of specific events, and local environmental signals to be assessed from the same archive.

We present a continuous ~37,000-year record of paleoenvironmental change inferred from physical, geochemical, and environmental magnetic analyses of sediment cores from Burial Lake, Arctic Alaska, with a well-constrained radiocarbon chronology determined from accelerator mass spectrometry (AMS), that provides one of the oldest continuous lacustrine records from eastern Beringia to date. Previous magnetic studies on Alaskan loess (Begét, 1990, 2001; Begét et al., 1990; Vlag et al., 1999; Liu et al., 1999; Lagroix and Banerjee, 2002; Muhs et al., 2003a; Muhs and Budahn, 2006; Evans et al., 2011) provide diagnostic magnetic parameters that allow locally weathered hematite-rich bedrock to be distinguished from ferrimagnetic (magnetite-rich) aeolian dust. Performing this study within a simple depositional basin with no direct inflow or glacial influence allows us to reconstruct the paleo-record of aeolian dust and its evolution for NW Alaska.

2. Regional setting

Burial Lake (68.43°N, 159.17°W) lies at 460 m above sea level in the Northwest Brooks Range, Alaska (Fig. 1). It is a small (~0.8 km^2), roughly circular lake, with a maximum depth of 21.5 m. The small (~3.3 km^2) catchment, which is perched above the surrounding tundra on a slight topographic high, has steep-sided embankments (3–5 m high) that extend along most of the lake's perimeter. The lake has no direct inflow and contains a small outlet stream on the southwest shoreline. Burial Lake is an oligotrophic, hydrologically open system, and is well mixed, with no evidence for year-round thermal or chemical stratification (Abbott et al., 2010). During the mid and late Pleistocene, mountain glaciers emanating from the Delong Mountains repeatedly dammed the Noatak River forming a series of large proglacial lakes with surface areas as large as 4400 km^2 (Hamilton, 2001) – collectively known as *Glacial Lake Noatak* (Hamilton and Van Etten, 1984). Glacial Lake Noatak appears not to have inundated Burial Lake since the Itkillik I (early Wisconsinan) glacial advance (Hamilton, 2010), and the lake remained free of glacial influence during the Last Glacial Maximum (LGM: 26.5–19 ka; Clark et al., 2009), lying just beyond the reach of mountain glaciers and Northern Hemisphere ice-sheet extent (Hamilton, 2001). Based on its isolated geographic setting and lack of fluvial input, we presume that sedimentation is influenced by aeolian deposition, with additional inputs derived from seasonal runoff and biogenic accrual.

3. Methods

3.1. Field methods

During the summer of 2010, three sediment cores ranging from 4.15 to 6.51 m in length were collected; two from the deep central basin (A10 and C10: 21.5 m water depth) and one nearer to the margin (D10: 8.5 m water depth) using a 2″ diameter square-rod Livingstone coring system designed to take 1 m successive drives. A larger, 2 5/8″ polycarbonate barrel was used to recover the

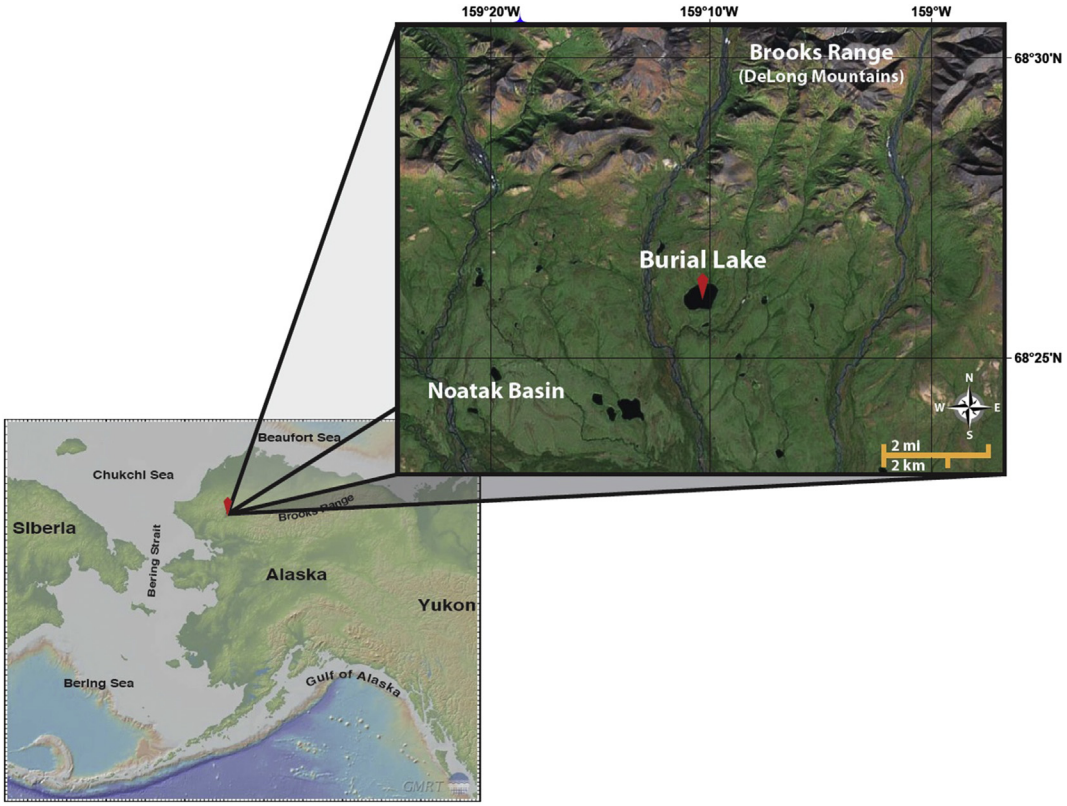

Fig. 1. Site location map. Burial Lake (68.43°N, 159.17°W) is located in the Noatak Basin in the northwest Brooks Range, Arctic Alaska, at the foot of the DeLong Mountains.

undisturbed sediment–water interface at each location. Overlapping sections assured complete recovery in the upper part of each record, but in order to achieve deeper core penetration, holes were cased with PVC pipe, restricting the ability to overlap drives in the lower portions of the records.

3.2. Physical and geochemical analyses

Whole cores were split, described, and subsampled using ridged plastic u-channels (2 × 2 cm cross-sectional area) at the University of Pittsburgh. Organic content and wet/dry bulk density were computed from standard loss on ignition (LOI) analysis, weight percent biogenic silica (BSi) was determined, and X-ray fluorescence (XRF) measurements provided major and minor elemental abundances (see Finkenbinder et al., this issue for detailed methodology). At the *Institut des sciences de la mer de Rimouski* (ISMER), in Rimouski (Quebec, Canada), u-channels were photographed using a high-resolution digital camera mounted on a GEOTEK™ Multi Sensor Core Logger (MSCL). Select samples were analyzed using smear-slides, and scanning electron microscope (SEM) images were acquired to visualize grain-specific traits and characterize the relative abundance of diatoms. Bulk physical grain size (including both lithogenic and biogenic fractions) was measured at 10 cm increments using a Beckman-Coulter™ LS 13320 laser diffraction analyzer. Grain size distribution and statistical parameters were calculated using Gradistat software (Blott and Pye, 2001). Computed Tomography (CT) scans on the u-channels were obtained at the *Institut national de la recherche scientifique, Centre Eau-Terre-Environnement* (INRS-ETE) in Quebec City, in order to visualize sedimentary structures, assess possible core deformation, and aid stratigraphic correlation. Following on methods provided by Duchesne et al. (2009) and Fortin et al. (2013), the topograms (scans in the longitudinal plane) were transferred into digital DICOM format using a standard Hounsfield scale (HU scale) (Hounsfield, 1973) from −1024 to 3071, where −1024 corresponds to the density of the air, 0 to the density of water, and 2500 to the density of calcite. The MATLAB™ code developed at ISMER removes effects of the plastic u-channel liner and air gaps from cracks in the sediment to allow for a more accurate HU calculation and a more realistic representation of changes in relative density down-core.

3.3. Rock magnetic measurements

Point source low-field magnetic susceptibility (k_{LF}) was measured on split cores at the University of Pittsburgh, at 2 mm intervals using a Bartington™ MS2 meter and MS2E1 sensor, mounted to a TAMISCAN-TS1 automatic stage conveyor. Rock magnetic properties were studied through progressive alternating field (AF) demagnetization of u-channel samples measured at 1 cm intervals using a 2G Enterprises™ model 755-1.65UC superconducting rock magnetometer at the Oregon State University *Paleo- and Environmental Magnetism Laboratory*. U-channel results were processed using UPmag software (Xuan and Channell, 2009).

After natural remanent magnetization (NRM) measurements (the paleomagnetic results of this study will be presented elsewhere), anhysteretic remanent magnetization (ARM) was induced at a peak AF of 100 mT with a 0.05 mT direct current (DC) biasing field and measured before and after AF demagnetization up to a peak AF of 100 mT at 5 or 10 mT increments. An initial isothermal remanent magnetization (IRM) was imparted with a DC field of 0.3 T using an impulse magnetizer designed for u-channel samples and measured after demagnetization at the same steps as the ARM. A second IRM imparted with a DC field of 1.0 T and considered to represent a saturation isothermal remanent magnetization (SIRM) was also measured after demagnetization at the same steps as the ARM. The response to these laboratory-applied magnetizations is not only a function of the concentration of ferrimagnetic material within the sample, but also of the sample's mineralogy and domain state (typically referred to as *magnetic grain size*). A variety of ratios can be used to provide information on the magnetic assemblages' mineralogy and grain size. Commonly used ratios and their definitions have been tabulated in previous studies (e.g. King and Channell, 1991; Stoner and St. Onge, 2007; Hatfield and Stoner, 2013). Here, we describe the ratios most important to this study.

Demagnetization ratios (e.g., $ARM_{30\ mT}/ARM_{0\ mT}$, or $SIRM_{30\ mT}/SIRM_{0\ mT}$) provide information on the coercivity of the sample, which is a reflection of magnetic grain size and/or mineralogy (Stoner and St-Onge, 2007). Higher values indicate higher coercivity, or finer grain size if the sample is of uniform ferrimagnetic mineralogy (Stoner and St-Onge, 2007). $ARM_{0\ mT}/SIRM_{0\ mT}$ is widely employed as a magnetic grain size indicator for magnetite, with finer grain sizes yielding larger values (Evans and Heller, 2003). The parameter derived by normalizing the IRM at 0.3 T by the SIRM at 1.0 T, sometimes referred to as a pseudo S-Ratio (St-Onge et al., 2003) is analogous to the S-ratio of Stober and Thompson (1979), and can be used to estimate the proportion of high to low coercivity magnetic mineralogies (e.g., the proportion of magnetite to hematite). Values closer to 1 denote an exclusively low coercivity ferrimagnetic mineral assemblage, such as magnetite, while lower values signify the presence of higher coercivity components, such as hematite (Thompson and Oldfield, 1986; King and Channel, 1991; Stoner and St-Onge, 2007). The "hard" IRM (HIRM) is a measure of the concentration of high coercivity material (e.g., hematite), and is here defined as an alternative optimized for u-channel measurements (Stoner and St-Onge, 2007): $HIRM = 0.5^{*}(SIRM - IRM@0.3T)$.

Hysteresis experiments on subsampled bulk material were carried out at ISMER on a Princeton Measurements Corporation™ MicroMag model 2900 alternating gradient force magnetometer (AGM) to assess both mineralogy and magnetic grain size. Hysteresis loops were corrected for paramagnetic/diamagnetic contributions, and the following values were derived: the coercivity of magnetic minerals (Hc), the coercivity of remnance (Hcr), the saturation magnetization (Ms), and the saturation remnance (Mrs).

IRM acquisition experiments were performed on select bulk samples using a Princeton Measurements Corporation™ MicroMag model 3900 vibrating sample magnetometer (VSM) at Western Washington University. Data were smoothed using a MATLAB™ loess filter, and IRM decomposition was performed using IRMUNMIX V2.2 (Heslop et al., 2002). Thermomagnetic analyses were attempted on four bulk samples to study the temperature dependence of k_{LF}, using an MS2WF Bartington™ instrument. Measurements were heated at 2 °C steps from room temperature (24 °C) up to 700 °C, and subsequently cooled to room temperature. Unfortunately, given the weak k_{LF} of Burial Lake sediments and the sample size limitations of the instrument, results were inconclusive with values varying around zero and showing no perceptible change with temperature; therefore, these data are not presented.

4. Age-model and composite depth

Down-core measurements and detailed core descriptions were used to characterize lithologic subunits and transitions, and place the deep basin cores, A10 and C10, on a common depth scale. The construction of the A10/C10 composite depth scale is outlined in Fig. 2. No stretching or squeezing of C10 drives was required to achieve a satisfactory match. Given the quality, continuity, and extent of the A10 data set, we focus on our results from the 6.51 m A10 core. The A10/C10 composite depth scale (referred to throughout as "depth") is utilized solely for the production of the

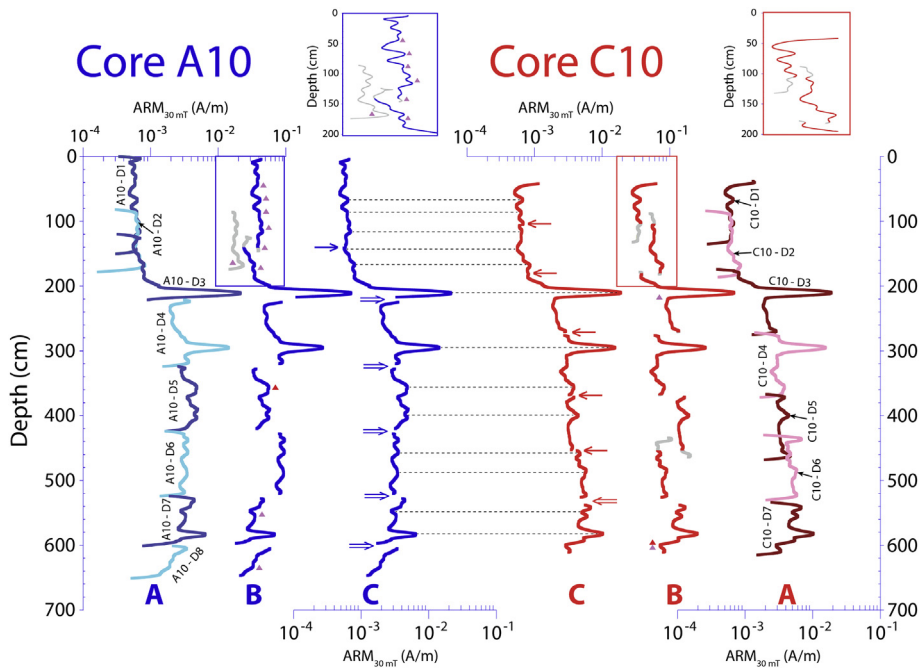

Fig. 2. A stratigraphic comparison and composite depth scale construction for cores A10/C10. $ARM_{30\ mT}$ values are plotted for cores A10 (**left side**) and C10 (**right side**) demonstrating their stratigraphic correlation on a common depth scale after C10 drives were "hung" to match the A10 record. Note, values are plotted on a log scale. **A**) Data for individual drives are shown in alternating colors, including magnetometer edge effects. **B**) Edge effects are removed and drives are offset to better show the alignment of features between overlapping drives. Grey segments show the drives or portions of drives that were not used in the final composite record of each core. Insets are shown for the upper 200 cm of each core (blue and red boxes), with values scaled to show variance. Locations of radiocarbon dates are shown, with pink triangles corresponding to accepted ages and red triangles corresponding to rejected ages. **C**) Data are recompiled to show the final composite record of each core. Locations of section breaks are shown for overlapping sections (→) and for sections that are either abutted or contain a data gap (⇒). Tie points show the agreement of features between the final composite versions of each core. Note, the final C10 composite record is not utilized in this report, and we mainly focus on results from the 6.51 m A10 core. The stratigraphic correlation does, however, allow us to incorporate C10 radiocarbon dates in the age-depth model for the A10 core. (For interpretation of the references to color in this figure legend, the reader is referred to the web version of this article.)

age-depth model, in which radiocarbon-dated samples were derived from both A10 and C10 cores (see Fig. 2).

AMS radiocarbon measurements were performed on 13 wood, seed, and plant macrofossil samples from cores A10 and C10 at the *Keck-Carbon Cycle AMS (KCCAMS) Facility* at the University of California, Irvine. Results are shown in Table 1 and Fig. 3. Size-dependent sample preparation backgrounds were subtracted based on measurements of ^{14}C-free (Queets-A) wood. Radiocarbon ages were calibrated using Calib 6.0 (Stuiver et al., 2005) and the IntCal09 calibration curve (Reimer et al., 2009).

Two out of the original 13 dates (UCIAMS #109363 and #89123; Table 1) were excluded prior to generating the age-depth model (Fig. 3). The first date at 359.5 cm appears anomalously young given its stratigraphic position, and was possibly contaminated by modern carbon during the combustion and graphitization of this very small (0.017 mgC) sample (Oswald et al., 2005), which approaches the threshold limit for AMS radiocarbon analysis at KCCAMS. Inclusion of this date would also invoke a sudden and drastic increase in sedimentation rate (reaching 1.51 m/ka), which is unsupported by additional radiocarbon constraints or lithologic evidence, and improbable given the depositional environment. The second date at 598 cm displays a slight age-reversal with an adjacent date (#89124; Table 1), though overlapping error bars suggest both are statistically sound age-control points. We exclude date #89123 based on its slightly broader uncertainty and lower carbon yield.

The *CLAM* software for "classical" age-depth modeling (Blaauw, 2010) was used to produce the "best fit" linearly interpolated age-model used in this paper (Fig. 3). The CLAM analysis performed

Table 1
AMS radiocarbon results based on macrofossils identified in deep basin cores A10 and C10, which were stratigraphically correlated to produce the composite depth scale (see Fig. 2). Radiocarbon ages were calibrated using Calib 6.0 (Stuiver et al., 2005) and the IntCal09 calibration curve (Reimer et al., 2009), and are reported at their 2σ confidence levels. Samples highlighted with an asterisk (*) are omitted from the age model with explanations in the text.

Sample ID (UCIAMS#)	Core-drive	Drive depth (cm)	Total depth (cm)	Material	^{14}C age (^{14}C yr)	Error (yr)	Calib 6.0 age (yr BP)
89197	A-10 D1	45.0	45.0	Plant material	2535	30	2493–2745
109361	A-10 D1	66.5	66.5	Wood	3635	25	3872–4074
116878	A-10 D1	87.5	87.5	Plant material	4910	90	5470–5896
89198	A-10 D1	111.0	111.0	Plant material	6345	25	7174–7410
109362	A-10 D1	141.5	141.5	Wood	8850	110	9564–10,205
89199	A-10 D2	84.0	166.0	Plant material	9760	40	11,134–11,244
89200	A-10 D3	54.0	173.5	Seed	10,085	45	11,398–11,959
89122	C-10 D3	45.0	219.0	Wood	13,670	30	16,657–16,978
* 109363	A-10 D5	35.5	359.5	Plant material	14,590	550	16,570–18,903
89201	A-10 D7	29.0	553.0	Seed	25,300	510	29,173–31,074
* 89123	C-10 D7	64.0	598.0	Plant material	31,290	300	35,085–36,475
89124	C-10 D7	72.0	606.0	Wood	31,090	210	35,036–36,313
89121	A-10 D8	35.5	636.5	Wood	32,150	240	35,699–37,342

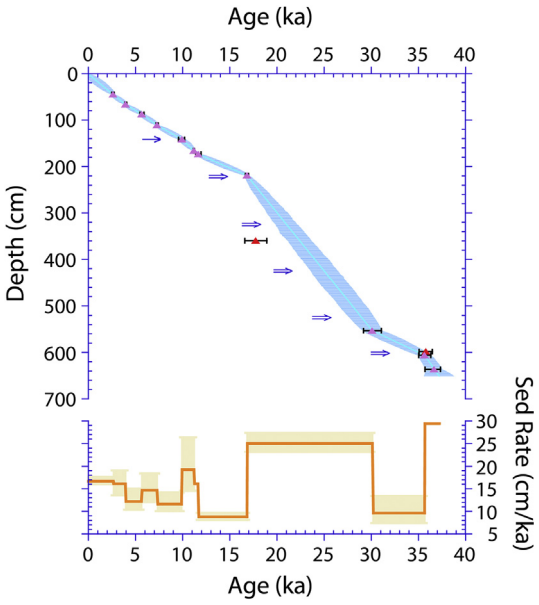

Fig. 3. AMS radiocarbon results based on macrofossils identified in deep basin cores A10 and C10, which were stratigraphically correlated to produce a composite depth scale. Radiocarbon ages were calibrated using Calib 6.0 (Stuiver et al., 2005) and the IntCal09 calibration curve (Reimer et al., 2009). Eleven calibrated median radiocarbon ages (pink triangles) are shown with associated 2σ error bars, as well as two dates, which were excluded from the age model (red triangles – see text for explanation). *CLAM* software for "classical" non-Bayesian age-depth modeling (Blaauw, 2010) was used to produce the "best fit" linearly interpolated age (cyan line) for the 6.51 m A10 core. Locations of A10 section breaks are shown for overlapping (⟶) and abutted (⟹) sections. The blue shaded envelope represents the maximum age variance computed between age control points based on the 2σ calibrated ^{14}C ages. It is the maximum AR1 normalized 1σ standard deviation computed from 10,000 Monte Carlo simulations following a random draw from a normal distribution (Marcott et al., 2013) with uncertainty between age control points based on a random walk model after Huybers and Wunsch (2004), using a "jitter factor" of 200. The orange line represents sedimentation rate over the ~37,000-year time interval with uncertainty generated using the 2σ calibrated age range of each age control point where feasible. (For interpretation of the references to color in this figure legend, the reader is referred to the web version of this article.)

1000 age model iterations based on repeated sampling of the calibrated age distributions for each radiocarbon sample to estimate the 'best fit' or weighted mean age for each depth. To further account for chronological uncertainty, we apply a Monte Carlo-based approach that perturbs the interpolated age-depth model 10,000 times following a random draw from a normal distribution between the 2σ calibrated ^{14}C ages (Marcott et al., 2013). The uncertainty between the age control points (Fig. 3) is modeled as a random walk, after Huybers and Wunch (2004), with chronological uncertainty assumed to be auto-correlated through time and modeled as a first order autoregressive (AR1) process.

5. Results

5.1. Sedimentology and lithostratigraphy

The sediment record from Burial Lake continuously spans the last ~37,000 years, with sedimentation rates (Fig. 3) ranging between 8.8 and 29.4 cm/ka, averaging 20.3 cm/ka for the whole record. The record shows distinct changes down-core from a homogenous grayish brown (5YR 3/2) to dusky brown (5YR 2/2), argillaceous silt sediment with higher organic carbon, low magnetic concentration, and high magnetic coercivity at the top of the core, to a dark yellow brown (10YR 4/2) to grayish brown (5YR 3/2), fine to medium sandy argillaceous silt with minor proportion of coarse sand and granules, lower organic carbon, higher magnetic concentration, and low coercivity below. Based on these changes, the record can be divided into three distinct lithologic subunits defined using down-core physical, geochemical, and magnetic properties (Fig. 4) that aid the paleo-environmental interpretation of the Burial Lake record. We note that subunit boundaries differ slightly between this study and the paleoclimatic interpretation of the Burial Lake sedimentary record presented by Finkenbinder et al., this issue. Despite our collaboration, this incongruence is to be expected given that both studies make use of independent data sets and focus on related, but distinctly different aspects and mechanisms of regional environmental change. The inclusion of environmental magnetic data sets in this study has particularly influenced our placement of lithologic boundaries, providing an added dimension for interpreting lithologic changes down-core as they relate to sediment sourcing over time.

5.1.1. Lithologic Subunit 1 (651–285 cm)

Subunit 1 corresponds to the glacial period (37.2–19.4 ka), and extends from the base of the core (651 cm) to 285 cm (Fig. 4). Sediments consist mainly of pale yellowish-brown (Munsell color: 10YR 6/2) to dark yellowish-brown (10YR 4/2) fine-grained silts and clay and a small fraction of sand and granules that exceeded the 2 mm measurement limit of the laser diffraction analyzer, which was sieved and removed prior to textural analysis. Mean physical grain size (Fig. 4) for Subunit 1 ranges between 4 and 10 μm. Faint banding is observed in CT images from this interval, and throughout the Burial Lake record (Fig. 4). CT density (324.4 ± 62.9 HU) and k_{LF} ($1.3 \times 10^{-5} \pm 0.3 \times 10^{-5}$) are relatively high and variable, while organic matter (8.1% ± 0.9%) and BSi (1.4% ± 0.4%) contents are relatively low (Fig. 4). These data are consistent with smear-slides and SEM images, which reveal sediment composed mainly of fine-grained lithogenic detritus, and containing a near absence of diatoms. Though BSi in Subunit 1 (Fig. 4) shows no significant long-term trend, organic matter (Fig. 4) generally increases downwards, while k_{LF} gradually decreases downwards. Other concentration-dependent magnetic parameters, ARM, IRM, and SIRM (Fig. 4) mimic k_{LF}, with relatively high and variable intensities, consistent with higher concentrations of ferrimagnetic material in this subunit. Ratios of $ARM_{30\ mT}/ARM_{0\ mT}$ and $SIRM_{30\ mT}/SIRM_{0\ mT}$ (Fig. 4; 0.49 ± 0.03, and 0.38 ± 0.04, respectively) suggest sediments in Subunit 1 are dominated by a low coercivity mineral assemblage, with values typical of magnetite. S-Ratios (Fig. 4) are high (0.93 ± 0.02), increasing up core to a maximum of ~0.96 near the top of Subunit 1, consistent with a high proportion of magnetite. Decreasing S-Ratios with depth (reaching ~0.86 at the base of the core) suggest an increasing proportion of high coercivity minerals (e.g. hematite) toward the bottom of the record.

While uncorrected hysteresis loops (Fig. 5) show high-field slopes indicative of paramagnetic contributions, slope-corrected loops (Fig. 5) are consistent with low coercivity ferrimagnetic contributions, with Mrs/Ms values mostly ranging between 0.1 and 0.3, and saturation fields mostly below 0.2 T (Day et al., 1977; Tauxe, 1993). Ratios of Mrs/Ms and Hcr/Hc (Fig. 5) indicate that samples from Subunit 1 fall within the pseudo single-domain (PSD) to just within the multi-domain (MD) fields for magnetite (Day et al., 1977).

Sub-centimeter scale, discrete peaks in magnetic parameters punctuate the record at 582, 294, and 210 cm (33.1, 19.8, and 15.8 ka, respectively) (Fig. 4). These are perhaps related to crypto-tephra deposits, though none of this relatively strong magnetic material could be isolated and therefore, their source remains unknown.

Sedimentation rates (Fig. 3) in Burial Lake are elevated (25.0–29.4 cm/ka) throughout most of the glacial period, with the exception of the interval between 30.2 and 35.6 ka, where they

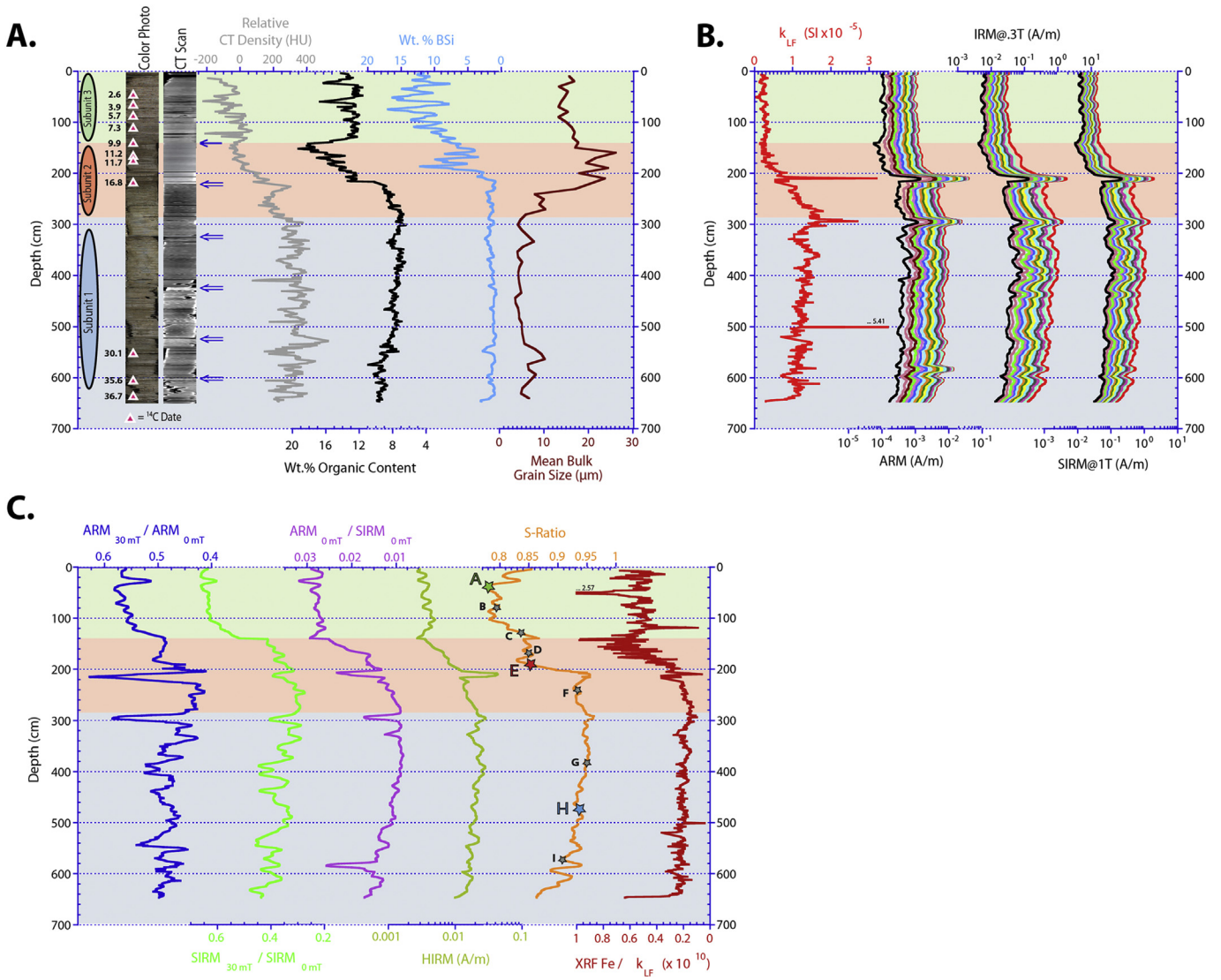

Fig. 4. Down-core physical, geochemical, and magnetic properties versus depth. **A**) Physical and geochemical properties: (from left to right) Color photo with radiocarbon ages (pink triangles) for reference, Computer Tomography (CT) image with locations of A10 section breaks for overlapping (⟵) and abutted (⟸) sections, relative CT density, organic content, biogenic silica (BSi), and mean bulk physical grain size. Lithologic subunits are designated by color: Subunit 1 (blue) from 651 to 285 cm, Subunit 2 (red) from 285 to 140 cm, and Subunit 3 (green) from 140 to 0 cm. **B**) Concentration dependent magnetic parameters: magnetic susceptibility (k_{LF}), anhysteretic remanent magnetization (ARM), isothermal remanent magnetization (IRM), and saturation isothermal remanent magnetization (SIRM), plotted with their respective alternating field (AF) demagnetization steps ranging from 10 to 80 mT. **C**) Magnetic ratios for coercivity/grain size/mineralogy: $ARM_{30\ mT}/ARM_{0\ mT}$, $SIRM_{30\ mT}/SIRM_{0\ mT}$, $ARM_{0\ mT}/SIRM_{0\ mT}$, hard isothermal remnant magnetization (HIRM), S-Ratios (stars and lettering indicate sample locations for IRM acquisition/decomposition, with enlarged colored symbols indicated representative samples from each subunit), and X-ray fluorescence (XRF) Fe/k_{LF}. Note some parameters are plotted on a log scale. (For interpretation of the references to color in this figure legend, the reader is referred to the web version of this article.)

appear to drop to 9.6 cm/ka. Timing of sedimentation rate changes and the magnitude of uncertainty are at least partially a function of the radiocarbon date locations, and without a better-constrained chronology through the glacial interval, it is difficult to address sedimentation rate in context with environmental change.

5.1.2. Lithologic Subunit 2 (285–140 cm)

Subunit 2, corresponding to the deglacial transition (19.4–9.8 ka), is characterized by a transitional lithology extending between 285 and 140 cm (Fig. 4). Lower sediments are dark yellowish-brown (10YR 4/2) in color, changing to a dusky-brown (5YR 2/2) at ~225 cm, and eventually grading to greyish-brown (5YR 3/2) in the upper part of the transition. Marked declines in CT density, k_{LF}, ARM, IRM, and SIRM (Fig. 4) are accompanied by increased organic content and BSi (Fig. 4). Sediments are still dominated by silts and clay, but mean physical grain size increases substantially, peaking around 160 cm at 26 μm (Fig. 4) with the addition of a fine to very fine sand fraction and an increased proportion of coarse to very coarse silt. As physical grain size samples were not pre-treated to remove biogenic components, the increase in grain size during this time interval may be attributed to the increased abundance of diatoms, which were often larger than lithic grains when observed through SEM imaging. Ratios of $ARM_{30\ mT}/ARM_{0\ mT}$ and $SIRM_{30\ mT}/SIRM_{0\ mT}$ (Fig. 4) increase through the transition, and since coercivity variations within these parameters are mainly limited to what can be achieved by AF demagnetization at low fields, the increase in coercivity is consistent with a fining of magnetic grain size, rather than a change in mineralogy. This is supported by increasing values of $ARM_{0\ mT}/SIRM_{0\ mT}$ (Fig. 4), as ARM is sensitive to fine-grained magnetite (Evans and Heller,

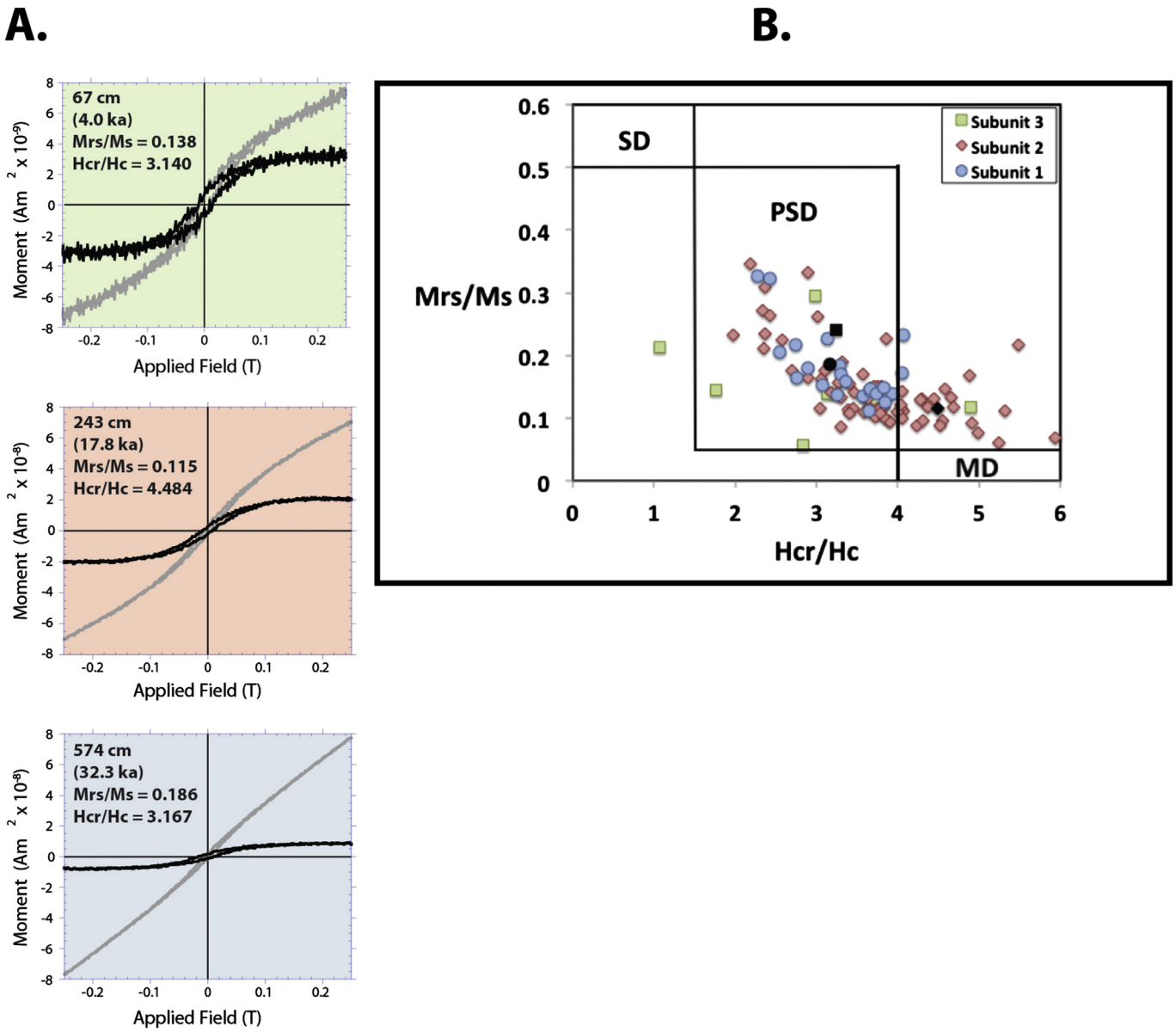

Fig. 5. Hysteresis results. **A**) Hysteresis loops generated from alternating gradient force magnetometer (AGM) measurements on representative samples from each lithologic subunit. Uncorrected loops are shown (grey lines) as well as those corrected for high-field paramagnetic/diamagnetic contributions (black lines). Shapes of loops demonstrate the presence of low coercivity ferrimagnetic minerals such as magnetite, and also exhibit paramagnetic contributions. Noisy loops in Subunit 3 are indicative of low ferrimagnetic magnetic concentration. **B**) Hysteresis ratios of Hcr/Hc and Mrs/Ms plotted according to Day et al. (1977) for a number of samples within each subunit, with theoretical domain state (magnetic grain size) boundaries drawn according to the behavior of pure magnetite (Day et al., 1977). Most samples fall within the PSD-MD magnetic grain size range including values derived from the hysteresis loops depicted here (black symbols), though scatter does occur – likely due to low ferrimagnetic concentration and/or high coercivity components.

2003). Bulk magnetic grain size is contrary to mean physical grain size (Fig. 4), however, the influence of biogenic contributions to bulk physical grain size as well as magnetic mineralogical changes on these ratios must be considered.

A distinct change in S-Ratios is observed to occur around 212 cm, (16 ka; Fig. 4). This is interpreted to result from a change in magnetic mineralogy (Thompson and Oldfield, 1986; King and Channel, 1991; Stoner and St. Onge, 2007). HIRMs (Fig. 4) decrease through this interval, as do k_{LF}, ARM, IRM, and SIRM, demonstrating the overall decrease in concentration of both the high and low coercivity magnetic components. Because the decrease in concentration of both low and high coercivity minerals is associated with increases in productivity indicators (Fig. 4), it results at least partially from organic/biogenic dilution of the detrital components. S-Ratios, on the other hand, are insensitive to organic/biogenic dilution, and sharply decline to ~0.83 (Fig. 4), reflecting an increase in the proportion of high coercivity minerals (hematite) relative to low coercivity minerals (magnetite) through this transitional subunit. As discussed above, magnetic grain sizes of the low coercivity component fine through the transition, a pattern inconsistent with diagenetic dissolution. S-Ratios slightly increase for the remainder of Subunit 2, but remain below 0.86. Sedimentation rates (Fig. 3) appear to decrease through the deglacial transition, averaging 18.3 cm/ka, and reaching their lowest overall values between 16.8 and 11.7 ka.

5.1.3. *Lithologic Subunit 3 (140–0 cm)*

Subunit 3, dating to the Holocene (9.8 ka – present), extends

from 140 cm to the top of the core (0 cm; Fig. 4). Sediments consist mainly of fine to very coarse silt with small contributions of very fine sand and clay – dusky-brown (5YR 2/2) at the base and grading to greyish-brown (5YR 3/2). Uppermost sediments are dark-yellowish brown (10YR 4/2). Mean physical grain size remains elevated (Fig. 4), ranging between 13 and 18 μm. A homogenous, fine-grained ferrimagnetic assemblage is suggested by higher values of $ARM_{0\ mT}/SIRM_{0\ mT}$, as well as $ARM_{30\ mT}/ARM_{0\ mT}$ and $SIRM_{30\ mT}/SIRM_{0\ mT}$ ratios, (0.55 ± 0.02 and 0.62 ± 0.03, respectively; Fig. 4). CT density is low and less variable (−47.1 ± 62.8 HU), along with k_{LF} ($0.26 \times 10^{-5} \pm 0.07 \times 10^{-5}$) and other concentration dependent magnetic parameters (Fig. 4). Organic content peaks near the boundary of Subunits 2 and 3 at 19.3% (Fig. 4), then slightly decreases until ~129 cm, but remains elevated (13.2% ± 1.1%) compared to previous subunits. BSi is also elevated (11.4% ± 2.4%), increasing steadily from the base of Subunit 3 before leveling off in the upper ~100 cm (Fig. 4). These data are consistent with smear-slides and SEM images that reveal an increased abundance of diatoms and organic detritus, relative to clastic mineral matter. Noisy hysteresis loops (Fig. 5) reflect the low ferrimagnetic concentrations in Subunit 3, which approach instrument limitations and result in somewhat scattered hysteresis results with respect to domain-state boundaries (Fig. 5).

S-Ratios (0.81 ± 0.02) decline abruptly again between 140 and 103 cm, reaching values as low as ~0.78 (Fig. 4). Values increase again in the upper ~35 cm, but do not exceed 0.85. Smaller values of XRF Fe/k_{LF} in Subunit 1 (Fig. 4) suggest the iron content of these sediments is more or less accounted for by k_{LF}, meaning that iron bearing minerals contribute heavily towards the total magnetic susceptibility. Conversely, the higher ratios observed during Subunits 2 and 3 reflect sediments that are high in iron, yet display weak values of k_{LF}. This "unaccounted" iron could be tied up in minerals like hematite, an iron oxide that is elevated in iron, but possesses a weaker k_{LF} (Dunlop and Özdemir, 2001), consistent with the increased proportion of high coercivity minerals. While not a definitive indicator of magnetic mineralogy, XRF Fe/k_{LF} provides complimentary geochemical evidence of a contrasting mineralogy between the upper and lower subunits. Sedimentation rates are also comparatively low (11.6–16.7 cm/ka) during the Holocene (Fig. 3), displaying a slight increasing trend from the early Holocene to present.

5.2. IRM acquisition/decomposition results

To further quantify the magnetic mineralogical changes, IRM acquisition curves were generated from subsampled material at nine down-core locations (Fig. 4). Representative normalized curves from each lithologic subunit are shown in Fig. 6. Results indicate similar coercivity distinctions as observed in the S-Ratios (Fig. 4), with samples from Subunit 1 acquiring magnetization more quickly than samples from Subunits 2 and 3, and displaying low coercivity behavior characteristic of ferromagnetic minerals (e.g., magnetite). All samples reach magnetic saturation within a narrow range of field intensities (1200–1400 mT), with samples from Subunits 2 and 3 saturating towards the high end of this range, indicating the presence of a high coercivity mineral assemblage (e.g. hematite). Regardless of the exact mineralogy, S-ratios and the following IRM decomposition results show it to be fundamentally distinct from the magnetite-rich sediments in Subunit 1.

IRM decomposition enables the separation of remanence-bearing sediments into their individual component contributions, allowing us to estimate the number of endmembers needed to explain the bulk magnetic properties of the sediments, and track relative changes in endmember contributions over time (depth). IRM decomposition results (Fig. 7) are based on smoothed input

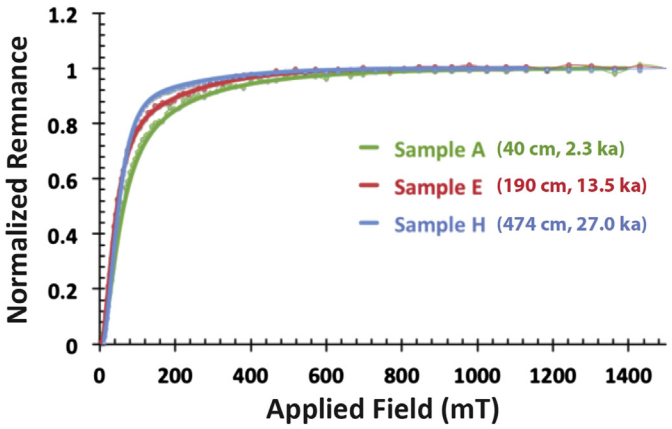

Fig. 6. Representative normalized IRM acquisition curves from Subunit 1 (H: 474 cm, 27.0 ka), Subunit 2 (E: 190 cm, 13.5 ka), and Subunit 3 (A: 40 cm, 2.3 ka). Sample A displays higher coercivity behavior than samples E and H, consistent with a distinctive change in mineralogy. Raw data points were smoothed using a MATLAB™ loess filter prior to IRM decomposition, as is indicated by the thick solid lines.

curves from Fig. 6, with results for all samples provided in Table 2. Smoothing was required because the extremely weak magnetization of these samples resulted in measurement noise. The consistency of results supports the interpretations. Burial Lake sediments are best described by a two-component model, with both low coercivity (component 1) and high coercivity (component 2) sources present throughout the record. The R^2 correlation of smoothed input data to the sum of one, two, three, and four components, are provided in Appendix A, supporting our use of a two-component model. Following on the principle of parsimony (Imbrie, 1963), which was specifically envisioned for the case of unmixing models, this provides the best-fitting, simplest, and most geologically meaningful solution.

Excluding two samples, which contained either excessive measurement noise (sample B), or a third low coercivity component (sample G), mean coercivities for component 1 (Table 2) are extremely consistent (44.0 ± 2.7 mT), suggestive of a common low coercivity mineralogy, and consistent with a fine-grained, PSD magnetite source. Mean coercivities for component 2 (Table 2; 270.2 ± 56.8 mT) are much higher, with increased variability perhaps indicating variable high coercivity sources, or an artifact induced by smoothing in the much noisier high coercivity range (Fig. 7).

Relative percent contributions depicted in Fig. 7 and Table 2 illuminate coercivity trends observed in S-Ratios (Fig. 4). Though high coercivity minerals are present throughout the record, their influence on S-Ratios is at times overshadowed by increased abundance of a low coercivity, ferrimagnetic mineralogy (e.g., magnetite). This observation is consistent with previous studies on S-Ratio sensitivity (e.g., Frank and Nowaczyk, 2008) that conclude an overwhelming percentage of hematite is needed to cause any major decrease in S-Ratios. Sample H (474 cm) from Subunit 1 provides an instructive example, containing an overwhelming 93.0% component 1 (compared with 7.0% component 2), corresponding to a high S-Ratio of 0.94. Only when component 1 contributions are reduced throughout Subunits 2 (e.g., sample E, 190 cm: 87.8%) and 3 (e.g., sample A, 40 cm: 68.2%), can component 2 drive S-Ratios towards lower values (0.85 and 0.78, respectively). The overall ~25% reduction in component 1 that occurs between samples H at 474 cm and sample A at 40 cm is consistent with the general decline in S-Ratios that occurs throughout Subunits 2 and 3. A 12.4% increase in component 1 is also observed to occur between samples I (574 cm) and H (474 cm), in keeping with increasing S-Ratios from the base of the core. Though components 1 and 2 refer specifically to IRM acquisition/decomposition results from a few

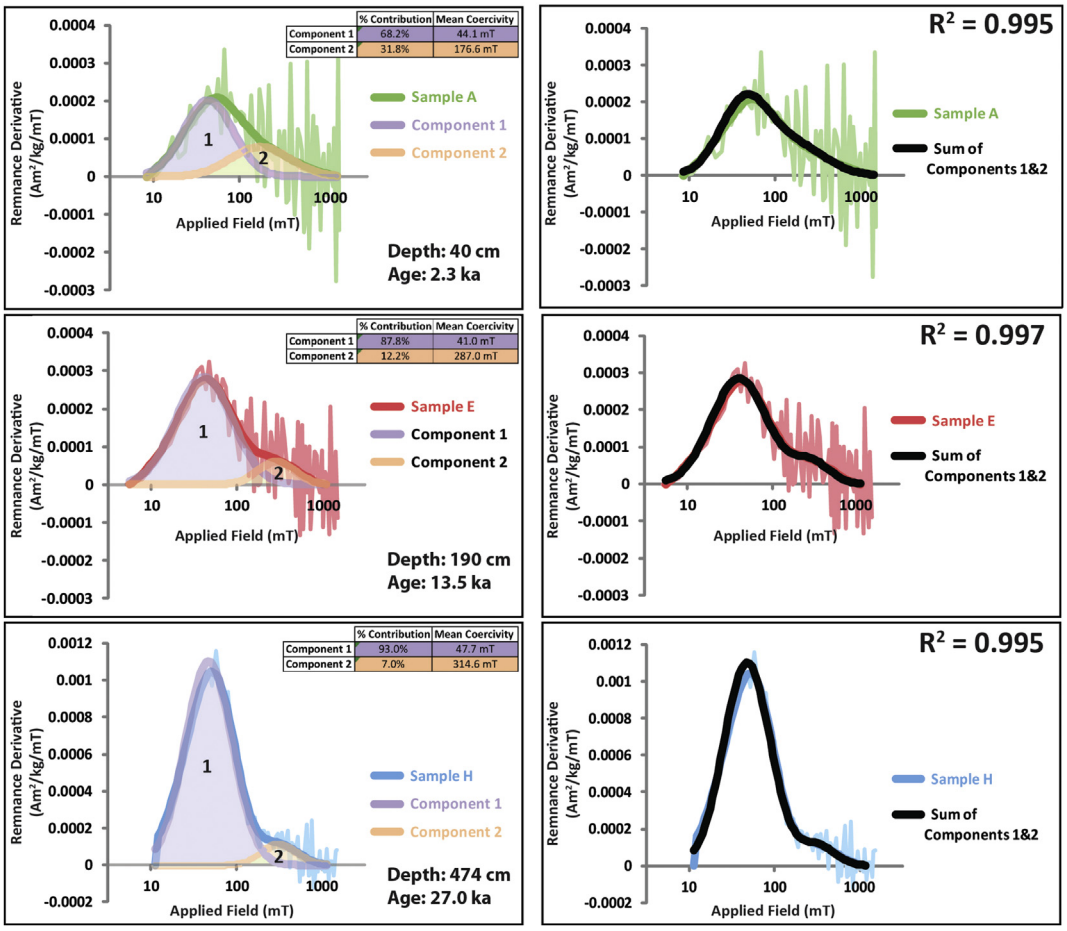

Fig. 7. Left column: IRM decomposition results based on smoothed data from Fig. 6. Non-normalized input data for representative samples from Subunit 1 (H: 474 cm, 27.0 ka), Subunit 2 (E: 190 cm, 13.5 ka), and Subunit 3 (A: 40 cm, 2.3 ka) were analyzed using IRMUNMIX V2.2 (Heslop et al., 2002) to decompose curves into their individual component contributions. Raw data is shown behind the smoothed curve for each sample. Note applied field is plotted on a log scale. Burial Lake sediments are best described by a two-component model with both low coercivity and high coercivity sources present throughout the record. Component 1 (shaded purple) is characteristic of low coercivity minerals (magnetite), and its relative abundance decreases by ~25% between Subunit 1 and Subunit 3. Component 2 (shaded orange) is characteristic of high coercivity minerals (hematite) and is ever-present throughout the record, but can easily be masked when component 1 is in high abundance (e.g., sample H in Subunit 1). Relative percent contribution and mean coercivity for each component is tabulated for each sample. Depths and ages for each sample are provided. **Right column**: The sum of components 1 and 2 compared against the smoothed input data, with R^2 values given for each sample, demonstrating excellent correlation. Raw data is again shown for reference behind the smoothed curves. (For interpretation of the references to color in this figure legend, the reader is referred to the web version of this article.)

discrete measurements, they are representative of the low and high coercivity mineralogies present in variable proportion throughout the Burial Lake record, identified through the number of different rock-magnetic observations pertaining to coercivity/mineralogy that are measured more continuously throughout each subunit (Fig. 4).

6. Discussion

6.1. Lithologic interpretation

Down-core physical, geochemical, and magnetic parameters are shown versus age in Fig. 8, allowing us to place our paleo-

Table 2
Summary of IRM decomposition results for samples A-I assuming a two-component model. Relative percent contribution for components 1 and 2 are given for each sample along with their mean coercivities. R^2 values are also given for the sum of components 1 and 2 compared against smoothed input data. Graphical results for samples H, E, and A are shown in Fig. 7, representing Subunits 1, 2, and 3, respectively. Note samples B and G appear anomalous, which can be attributed to measurement noise and/or better representation using a three-component model (see text for further explanation).

Sample (depth)	% Component 1	% Component 2	Mean coercivity component 1 (mT)	Mean coercivity component 2 (mT)	Sum of components 1&2 R^2 correlation to smoothed input data	
A (40 cm)	68.2	31.8	44.1	176.6	0.995	* Displayed above
B (80 cm)	43.4	56.6	38.0	105.6	0.972	* Noisy data
C (130 cm)	74.7	25.3	42.1	239.1	0.994	
D (170 cm)	89.3	10.7	43.5	303.7	0.998	
E (190 cm)	87.8	12.2	41.0	287.0	0.997	* Displayed above
F (241 cm)	94.1	5.9	42.0	339.2	0.996	
G (384 cm)	56.1	43.9	44.2	60.2	0.992	* Best fit by 3 components.
H (474 cm)	93.0	7.0	47.7	314.6	0.995	* Displayed above
I (574 cm)	80.6	19.4	47.7	231.5	0.987	

environmental results in the context of time. The pattern of variability observed in the Burial Lake record, with high concentrations of low coercivity magnetic minerals and a low proportion of high coercivity minerals in the lower part of the record, transitioning to reduced concentrations of low coercivity minerals and an increased proportion of high coercivity minerals at the top of the record, could be explained by diagenetic alteration through post-depositional magnetite dissolution (e.g., Snowball, 1993), a change in sediment source(s) (e.g., Thompson and Oldfield, 1986), or some combination of both. Although negative correlations between organic carbon and magnetic concentration are consistent with diagenetic alteration, they are also consistent with the general climatic transition from glacial to interglacial conditions. As Burial Lake is oligotrophic, hydraulically open, and is well oxygenated with no evidence for significant stratification, it fits phase 1 conditions of Evans and Heller (2003), suggesting sediments are unlikely to have undergone significant magnetic dissolution. Additionally, there is little physical evidence (e.g., laminations, gas production, hydrogen sulfide smell, significant color changes, or pyrite formation) at any point in the record to suggest significant reducing and/or sulfidic conditions generally associated with magnetic dissolution (e.g., Karlin and Levi, 1983; Canfield and Berner, 1987; Anderson and Rippey, 1988; Rowan et al., 2009). X-Ray diffraction (XRD) results from Finkenbinder et al., (this issue) also show no indication of pyrite formation. There is no progressive decrease in intensity and/or corresponding increase in ferrimagnetic grain-size with depth in Subunit 3 (Fig. 4), as would be expected for magnetic dissolution (Karlin and Levi, 1983; Anderson and Rippey, 1988; Snowball, 1993). The ferrimagnetic grain size in Subunit 3 is finer than that observed deeper in the core, also inconsistent with magnetic dissolution of a similar parent material (Karlin and Levi, 1983; Anderson and Rippey, 1988; Snowball, 1993).

On the basis of these observations, the rock magnetic variability and distinct shift in mineralogy observed in the Burial Lake record is more likely derived from variations in sediment sources, which we suspect reflect local versus far-field (aeolian) material. We interpret the low coercivity ferrimagnetic (e.g., magnetite) component to reflect the input of aeolian dust based on the following cumulative reasoning:

1. A low coercivity magnetic mineralogy dominates glacial period sedimentation in Burial Lake, (i.e., Subunit 1; Fig. 8), and enhanced glacial-age loess production is well supported, with ubiquitous deposits found throughout Alaska (Péwé, 1955; Muhs et al., 2003a, 2003b).
2. Glacial-age sediments from Burial Lake have comparable magnetic characteristics to Alaskan loess (Figs. 5–8; Table 2), which contains significant quantities of magnetite, contributing to high values of k_{LF}, and coercivity similar to that of component 1 (Fig. 7) (Begét, 1990, 2001; Begét et al., 1990; Vlag et al., 1999; Liu et al., 1999; Lagroix and Banerjee, 2002; Muhs et al., 2003a; Muhs and Budahn, 2006; Evans et al., 2011).
3. Sedimentation in Burial Lake during the glacial period is characterized by extensive fine-grained deposition of silts and clays with a mean physical grain size of 4–10 μm (Fig. 8). This is within the lower grain size range of the Alaskan loess (Muhs and Budahn, 2006), and consistent with aeolian deposition.
4. Detrital flux ($F_{detrital} = SR^*[BD^*(100\% - \%OM - \%BSi)]$), calculated by removing weight percent organic matter (OM) and biogenic silica (BSi) contributions from total dry bulk density (BD), and factoring in sedimentation rate (SR), shows that mineralogenic input was approximately four and half times greater during the glacial period than in the Holocene, consistent with the gradual diminished relative contribution of low coercivity ferrimagnetic components and the decrease in S-Ratios through the deglacial transition (Figs. 7 and 8).
5. Based on its regional geographic setting, Burial Lake appears sensitive to aeolian deposition. Given its relatively small watershed and lack of inflowing streams, the only means to achieve increased detrital flux during the glacial period (other than increasing dust flux) would be to increase precipitation and spring runoff. This conflicts with widespread evidence for prevailing xeric conditions over the glacial-age landscape of interior Alaska (Hopkins, 1982; Abbott et al., 2000; Finkenbinder et al., 2014).
6. Sedimentation rates are comparatively low during the Holocene (Fig. 3), and the concentration of the low coercivity magnetic component is diminished (Fig. 7), although it still accounts for the bulk of the magnetization in Holocene sediments. Again, based on regional geography, Burial Lake likely still remains sensitive to aeolian deposition. While less extensive and episodic in nature, Alaskan loess deposition continued even after the LGM, with deposits as recent as ~3000 ^{14}C yr BP found at Delta Junction, south of Fairbanks (Muhs et al., 2003a). Modern dust storms are common in Alaska during the snow-free months of spring, summer, and early fall (Begét, 2001). In some areas, river bars exposed to wind in winter can cause dust to accumulate in winter snowpack before melting out in the spring (Péwé, 1955).

For the following cumulative reasoning, high coercivity material is interpreted as a locally-derived source, weathered from surrounding uplands and transported to Burial Lake during seasonal runoff events:

1. Though variable, high coercivity material is present throughout all parts of the Burial Lake record (Fig. 7, Table 2), and requires an active sediment source irrespective of the drastic environmental changes associated with the glacial-interglacial transition, and therefore, must be immediately available from the local catchment.
2. The Brooks Range, while geologically diverse, has been shown to contain significant high coercivity mineral concentrations within the Paleozoic and Mesozoic sedimentary and metasedimentary strata that comprise regional bedrock topography (Slack et al., 2004; Mayfield et al., 1984; Ellersieck et al., 1984). Among such deposits are large outcroppings of the Kayak shale (early Mississippian), the same friable and highly oxidized (i.e., hematite bearing) material responsible for the reddish hue in sediments from Blue Lake (Bird et al., 2009) in the central Brooks Range near Atigun Pass.

Given these deductions, we suggest that S-Ratios, though only a measure of relative proportion, are a sensitive indicator for dust input to Burial Lake, with higher values indicating periods of increased accumulation, and lower values indicating periods of diminished flux, while IRM acquisition/decomposition allows for background levels of high coercivity material to be discerned throughout the record.

6.2. Local and far-field sources of dust, timing of deposition, and potential forcing mechanisms

There are three plausible ways in which aeolian dust could be made available for transport to Burial Lake: **1**) Sea level lowering could expose large portions of the continental shelves, providing a potential far-field source of dust to Burial Lake; **2**) Expansion of alpine glaciers in the Brooks Range or elsewhere could also generate a potential local revenue of dust (though it would need to

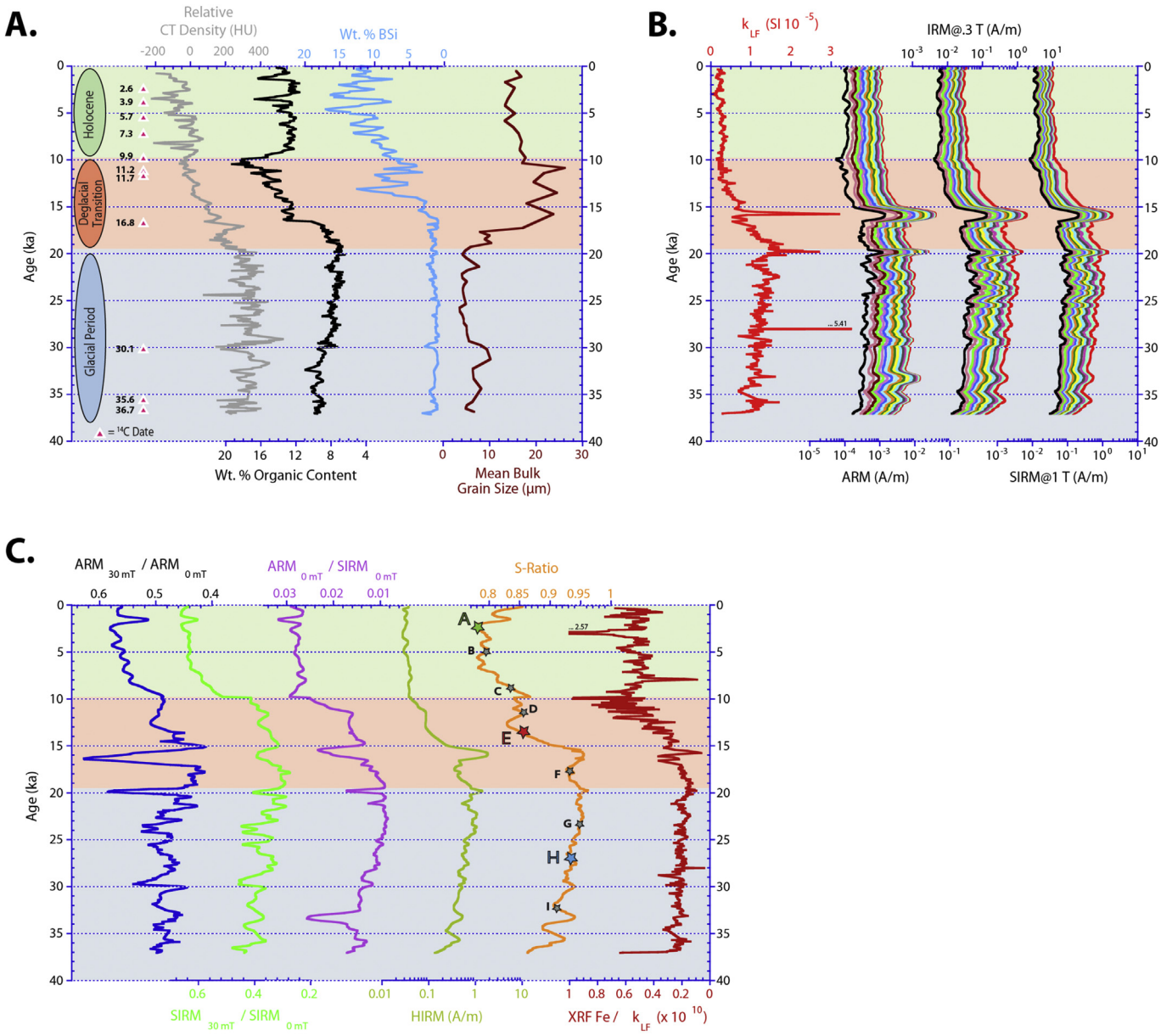

Fig. 8. Down-core physical, geochemical, and magnetic properties versus age. **A**) Physical and geochemical properties: (from left to right) Radiocarbon ages (pink triangles) for reference, relative CT density, organic content, biogenic silica (BSi), and mean bulk physical grain size. Lithologic subunits are designated by color and are now labeled in terms of the time period they represent: The last glacial period (blue) from 37.2 to 19.4 ka, the deglacial transition (red) from 19.4 to 9.8 ka, and the Holocene (green) from 9.8 ka to present. **B**) Concentration dependent magnetic parameters: Magnetic susceptibility (k_{LF}), anhysteretic remnant magnetization (ARM), isothermal remnant magnetization (IRM), and saturation isothermal remnant magnetization (SIRM), plotted with their respective alternating field (AF) demagnetization steps ranging from 10 to 80 mT. **C**) Magnetic ratios for coercivity/grain size/mineralogy: $ARM_{30\ mT}/ARM_{0\ mT}$, $SIRM_{30\ mT}/SIRM_{0\ mT}$, $ARM_{0\ mT}/SIRM_{0\ mT}$, hard isothermal remnant magnetization (HIRM), S-Ratios (stars and lettering indicate sample locations for IRM acquisition/decomposition, with enlarged colored symbols indicated representative samples from each subunit), and X-ray fluorescence (XRF) Fe/k_{LF}. Note some parameters are plotted on a log scale. (For interpretation of the references to color in this figure legend, the reader is referred to the web version of this article.)

be weathered from localized low coercivity bedrock to fit our description of component 1); and **3**) A dry and windy environment with little vegetative cover could expose the landscape to deflation, generating a widespread source of dust without the need to invoke sea level *or* glacial activity. In the remainder of this study, we provide a paleo-environmental interpretation of the Burial Lake record, devoting particular attention to the timing and extent of dust deposition as depicted by the S-Ratio proxy so as to distinguish the mechanism(s) responsible for increased or decreased dust input to Burial Lake, and therefore identify or exclude potential sources.

6.2.1. The last glacial period (Subunit 1) 37.2–19.4 ka

S-Ratios are highest and magnetic concentrations are greatest during the last glacial period (Fig. 8), and reflect a general increasing trend in dust accumulation from moderate levels in the earliest portion of the record during Marine Isotope Stage 3 (MIS-3; i.e., prior to ~30 ka), reaching a maximum at the height of the global LGM (19–20 ka). Fine-grained, lithogenic sediments with relatively high CT density and increasing values of k_{LF} (Fig. 8) are consistent with increasing accumulation of aeolian dust. Low organic matter (Fig. 8) and the general absence of macrofossils for AMS radiocarbon analysis between ~30 and ~17 ka (Fig. 3), suggest the

surrounding landscape was largely devoid of substantial vegetation, indicating a windswept tundra environment that was colder and drier than present. Low BSi (Fig. 8) suggests diminished lake productivity due to cold conditions with a short, ice-free summer season, along with potentially turbid and/or nutrient depleted waters. Abbott et al. (2010) determined that a depositional hiatus in the shallower portions of Burial Lake occurred between 33.0 and 24.3 ka (ages recalibrated using Calib 6.0 and the IntCAL09 calibration curve; Finkenbinder et al., this issue), corresponding to a significant drop in lake level from decreased moisture availability.

Proxy data from Burial Lake are consistent with evidence elsewhere in the region depicting extremely cold, arid, and windy conditions leading up to the LGM (Hopkins, 1982; Muhs et al., 2003a; Abbott et al., 2000, 2010; Kurek et al., 2009; Finkenbinder et al., 2014), highlighting the potential for significant landscape deflation and production of dust. Though loess production and windiness appear to increase, Muhs et al. (2003a) note surprisingly little accumulation of loess during the LGM, which they attribute to sparse vegetation and limited ground surface roughness. Though these attributes may inhibit terrestrial loess accretion, they would not necessarily prohibit deposition in lakes. Burial Lake S-Ratios may therefore offer a more accurate portrayal of dust production during the LGM, further demonstrating the advantages lacustrine records hold over traditional terrestrial loess deposits.

Bracketing radiocarbon ages of 30 and 13 ka in the central (Hamilton, 1982) and western (Hamilton, 2001) Brooks Range, constrain the timing of the subsequent Itkillik II (late Wisconsinan) glaciation, which reached its maximum extent between 27 and 25.5 ka (Fig. 9; Briner and Kaufman, 2008). Though extensive in the eastern and central parts of the Brooks Range, growth of alpine glaciers (and the potential for dust generation) became progressively more restricted towards the west, primarily due to the lower-lying topography of mountain valleys (Hamilton and Labay, 2011). Therefore, many alpine valleys in the western Brooks Range did not support glaciers of Itkillik II age (Hamilton and Labay, 2011). This, combined with the fact that S-Ratios do not diminish in response to waning Brooks Range glaciers from their maximum Itkillik II extents (they in fact continue to increase; Fig. 9), suggests that local glaciers likely did not contribute substantially to the supply of dust deposited in Burial Lake during the glacial period, or at least cannot be held accountable for the increasing trend in S-Ratios leading up to the LGM (Fig. 9).

Increased exposure of Beringian continental shelves from rapidly declining sea level may help to explain the increase in dust input over the glacial period, particularly considering that newly exposed coastline would likely have lacked substantial vegetative cover and been subjected to the same arid and windy conditions that persisted in the continental interior. A marine source has been inferred for glacial-age loess found in coastal locations along the Seward Peninsula, in USGS marine sediment cores from Norton Sound, and in Zagoskin Lake on St. Michael's Island (Muhs et al., 2003b). While these sites are limited to the western coast of Alaska, it is not unreasonable to think that winds could transport such material further inland. If continental shelves are viable sources of far-field dust, the surface area over which dust could be generated is massive in comparison to the relatively small footprint of mountain glaciers.

In comparing Burial Lake S-Ratios to relative sea level (Fig. 9; Clark et al., 2009) we observe only a moderate amount of dust accumulation occurring in the earliest part of the record, during MIS-3, in keeping with somewhat elevated sea level (roughly 70 m below present). As sea level declined, subaerial extent of continental shelves increased until sea level reached its lowest position (−123 m) at approximately 21 ka (maximum low-stand shelf exposure is depicted in Fig. 10). S-Ratios respond accordingly, reflecting an increase in dust input to Burial Lake.

6.2.2. The deglacial transition (Subunit 2) 19.4–9.8 ka

The lithologic transition, here characterized by decreasing magnetic concentration and CT density, accompanied by rising organic content and BSi (Fig. 8), is commonly observed in sediment records that span the glacial/interglacial transition. The beginning of the transition (19.4 ka) is coincident with the onset of Northern Hemisphere deglaciation (Clark et al., 2009, 2012). At Burial Lake, rising lake levels between 20.0 and 19.0 ka indicate increasing effective moisture (Abbott et al., 2010), while chironomids indicate increasing summer temperatures by 17.0 ka (Kurek et al., 2009), consistent with the observed rise in aquatic productivity, as evidenced by organic content and BSi (Fig. 8). Concentration dependent magnetic parameters decrease (Fig. 8), partially in response to organic/biogenic dilution of lithogenic sediments. However, dwindling sedimentation rates (Fig. 3) imply a decline in detrital flux as well, which S-Ratios (Fig. 8) suggest is in large part due to a reduction in low coercivity aeolian dust contribution. As many of the harsh conditions, once favorable to landscape deflation and production of dust during the glacial period, were ameliorated following the LGM, dust sources were effectively shut off from Burial Lake, permitting Holocene sedimentation to be dominated by local high coercivity input.

Although Burial Lake begins to respond to global climate changes at ~19.6 ka (Finkenbinder et al., this issue), the major decrease in S-Ratios that commences by ~ 16 ka, is broadly synchronous with the onset of the Bølling interstadial at 14.7 ka (Rasmussen et al., 2006), identified in $\delta^{18}O$ temperature proxy records from the North Greenland Ice Core Project (NGRIP) ice cores (Fig. 9; NGRIP members, 2004), and in tune with rising summer insolation (Fig. 9; Berger and Loutre, 1991). This is consistent with regional proxy data that reflect a local expression of Bølling warming and a rapid climatic teleconnection between the North Atlantic and North Pacific sectors (Broecker, 1994; Mikolajewicz et al., 1997; Hostetler et al., 1999; Davies et al., 2011; Praetorius and Mix, 2014). A rapid ~18 m rise in water levels at Birch Lake, south of Fairbanks at ~15 ka (Fig. 9; Abbott et al., 2000) and rising and higher lake levels at nearby Harding Lake by ~14 ka (Finkenbinder et al., 2014) indicate increased moisture availability. In addition, numerous other small, shallow lakes in Alaska began accumulating sediment between 15 and 13 ka (e.g., Ager, 1975; Bigelow, 1997; Bigelow and Edwards, 2001; Carlson and Finney, 2004). In summary, available evidence suggests that the landscape response to a more amiable climate may explain the reduction in dust input to Burial Lake during the deglacial transition. S-Ratios make a brief return to higher values between 12.6 and 9.8 ka, broadly coinciding with a period of fluctuating water levels in Birch Lake (Fig. 9; Abbott et al., 2000). Lower water levels in Lake of the Pleistocene (Nikivlik Lake) on the Arctic Foothills between 11,000 and 10,000 ^{14}C yr BP (~12,900 to ~11,600 cal yr BP; Mann et al., 2002) indicate a return to slightly drier conditions and increasing dustiness during the later stages of the transition. Bigelow et al. (1990) identified an increase in wind intensity between 13 and 12.6 ka from grain size variations in loess sequences along the Nenana River, which is in general agreement with this period of renewed dust deposition at Burial Lake.

Unlike the relationship observed in the glacial period, the glacial chronology of the Brooks Range during the transition is at times in phase with S-Ratios, and therefore we are unable to rule out alpine glaciers as potential mediators of dustiness in the Noatak Basin. The time–distance diagram for glaciers in the Brooks Range (Fig. 9; Briner and Kaufman, 2008) demonstrates that Itkillik II advances had largely withdrawn by the time of the first drop in S-Ratios at 16 ka. Accordingly, Hamilton (1982) observed that alluviation of

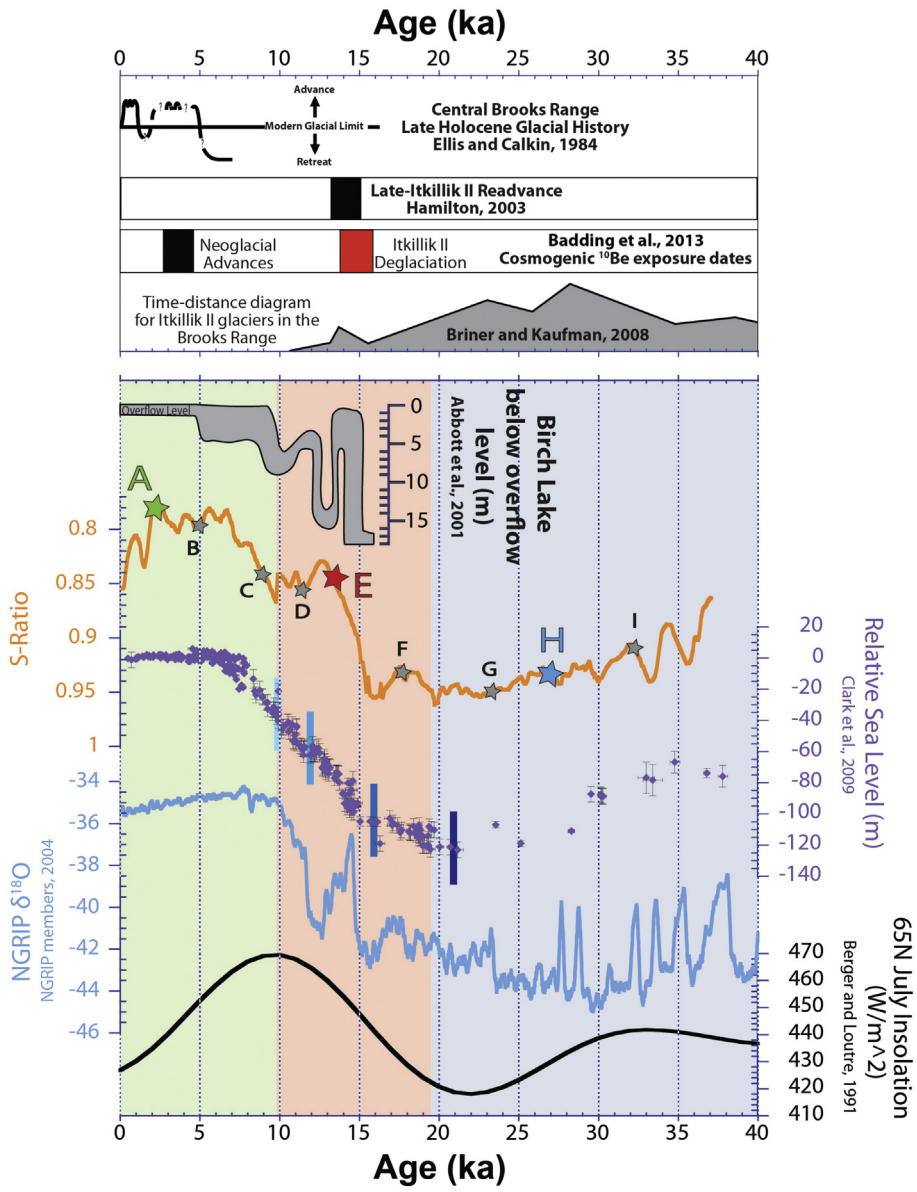

Fig. 9. Comparison of Burial Lake S-Ratios with proxy data for regional paleoclimate, glacial history of the Brooks Range, and relative sea level shown on a calibrated age scale. **Upper panel**: (from top to bottom) Lichen-inferred late Holocene glacial history of the central Brooks Range (Ellis and Calkin, 1984), Timing of the late-Itkillik II readvance (Hamilton, 2003), Timing of ice-retreat (red bar) and Neoglacial advances (black bar) in the north-central Brooks range as delimited by cosmogenic ^{10}Be exposure dating (Badding et al., 2013), Time-distance diagram for Itkillik II glaciers in the Brooks range (Briner and Kaufman, 2008). **Lower panel**: (From top to bottom) Lake-level reconstruction for Birch Lake (Abbott et al., 2001), Burial Lake S-Ratios (stars and lettering indicate sample locations for IRM acquisition/decomposition, with enlarged colored symbols indicated representative samples from each subunit), Relative sea level (Clark et al., 2009), NGRIP δ^{18}O (NGRIP members, 2004), Mid-month July solar insolation reconstructed for 65°N (Berger and Loutre, 1991). Colored vertical bars on the sea level curve correspond to the paleo-shoreline bins shown in Fig. 10. (For interpretation of the references to color in this figure legend, the reader is referred to the web version of this article.)

outwash streams in the Koyakuk River area on the south side of the range had ceased by 15 ka. Cosmogenic ^{10}Be exposure dating within the Kurupa and Antigun River valleys in the north-central Brooks Range shows evidence for ice retreat from the northern range prior to 15.9 ka, with glaciers disappearing entirely, or retreating into individual cirques by 13.8 ka (Fig. 9; Badding et al., 2013). Diminished glacial silt production from local glaciers could therefore elucidate the major coercivity change that we observe in Burial Lake at around the same time. Still, this would imply that dust from nearby glaciers is magnetically distinct from terrestrial runoff derived from the same general area (i.e., low coercivity vs. high coercivity), a perplexity that leads us to favor a more widespread or far-field diminishing source of dust. The lack of evidence for ice advance between 12.6 and 9.8 ka, suggests that general aridity and an increase in wind intensity are more likely responsible for dust emissions during this time.

Rising sea level and the rapid inundation of continental shelves may be largely responsible for a reduction in far-field derived dust input to Burial Lake, and also may explain the delayed response of S-Ratios from the start of the deglacial transition and the initial rise in summer insolation (Fig. 9). Although sea level began to rise ~21 ka (Fig. 9; Clark et al., 2009), S-Ratios do not appear to respond until 16 ka. The corresponding ~18 m rise in sea level, however, translates to a rather small surface area reduction of the continental shelf, thus subtracting little from their total potential generation of dust. This is well illustrated in Fig. 10, which shows

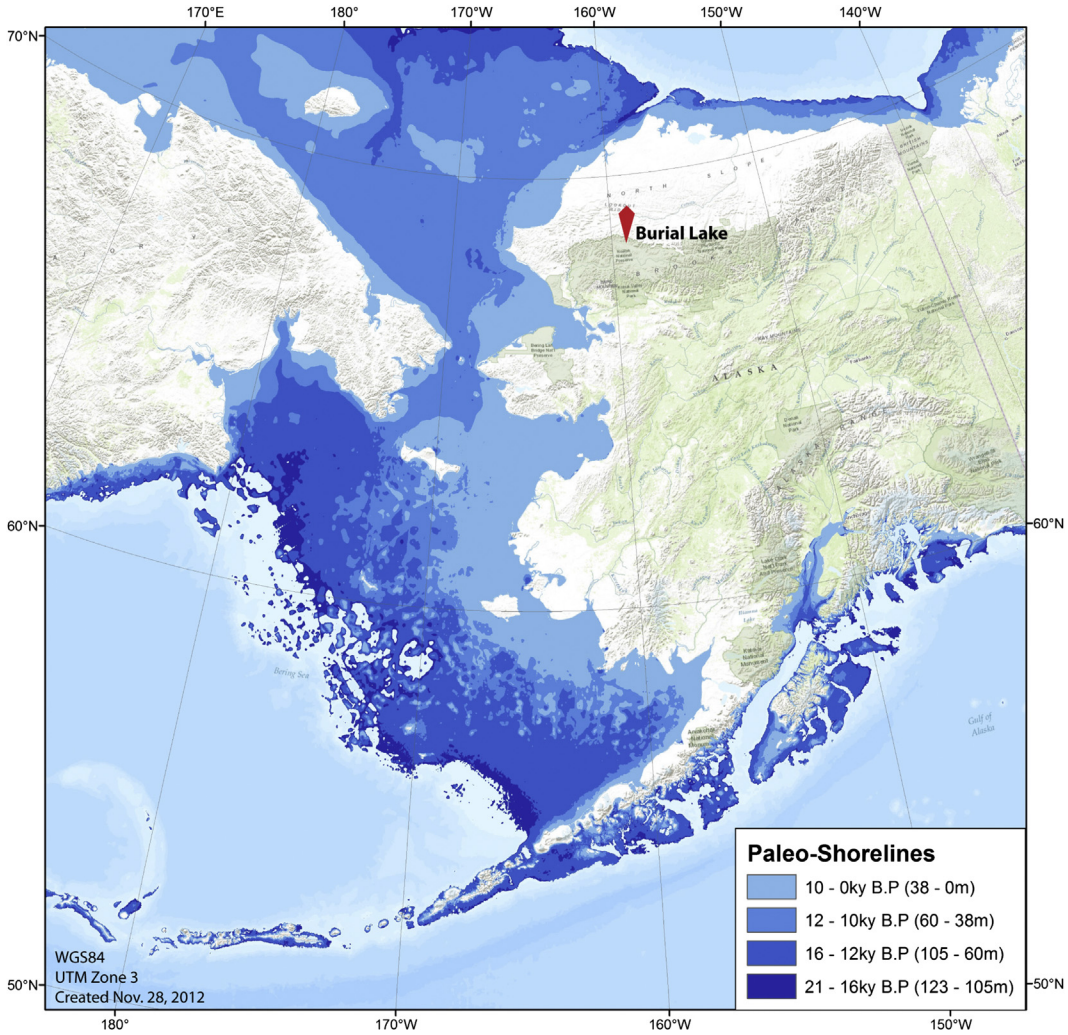

Fig. 10. Paleo-shoreline map of Beringia showing sea level rise and inundation of Beringian continental shelves from the LGM sea level low-stand (~21 ka) to present. Contours correspond to timing of major changes in S-Ratios at ~16, ~12, and ~10 ka (see Fig. 9).

paleo shorelines contoured according to the timing of major changes in S-Ratios, constructed using global multi-resolution topography (GMRT) from Ryan et al. (2009) and sea level estimates from Clark et al. (2009). The ~45 m of rise between 16 and 12 ka (Fig. 9), however, inundated a significant portion of Beringia (Fig. 10), and likely had a greater impact on dust availability and the magnetic proportions in Burial Lake. While sea level appears to maintain a higher order control on dust availability, it does not fully describe S-Ratios over the entirety of the transition. For example, the return to slightly drier and dustier conditions at Burial Lake between 12.6 and 9.8 ka occurs despite a ~22 m rise in sea level (Fig. 9), and a significant loss in land area (Fig. 10). Regional glacial isostatic adjustment (GIA) may have had significant effects on paleo-topography during the deglacial transition (Milne and Mitrovica, 2008), and should ultimately be considered in any quantitative evaluations of the timing and area extent of potential dust sources on continental shelves with respect to sea level rise.

6.2.3. *The Holocene (Subunit 3) 9.8 ka – present*

S-Ratios decrease again between 9.8 and 6.7 ka, attaining their lowest values in the mid-Holocene and implying a continued diminishing input of dust (Fig. 8). Values remain low and stable throughout the mid-Holocene, but increase again between ~2 ka and the present, suggesting a slight recent intensification of dustiness in the late Holocene (Fig. 8). Low CT density and low magnetic concentration observed throughout the Holocene interval (Fig. 8) is interpreted largely as a function of dilution from high organic matter and rising BSi as well as reduced input of the magnetically stronger low coercivity fraction (Fig. 8). Along with the general abundance of macrofossils for AMS radiocarbon analysis (Fig. 3), these data are characteristic of a warmer, more quiescent Holocene environment, with increased terrestrial and aquatic productivity, and enhanced precipitation.

Proxy data from Burial Lake support existing evidence for continued climatic amelioration during the Holocene. The peak in organic content at ~10.5 ka (just before the Holocene interval; Fig. 8) roughly coincides with peak summer insolation (Fig. 9; Berger and Loutre, 1991) and with the reopening of the Bering Strait at around 11 ka (Elias et al., 1997), which likely facilitated the transport of maritime air masses into interior Alaska. Birch Lake displays evidence for rising lake levels, approaching overflow conditions between 10 and 9 ka (Fig. 9), indicating an increase in effective moisture (Abbott et al., 2000). These conditions are again likely to have prevented landscape deflation, further reducing dust emissions, and contributing to the early to mid-Holocene decline in S-Ratios.

Following the readvance of glaciers between 15.1 and 13.3 ka (Fig. 9; Hamilton, 2003), no further Itkillik II glacial activity is reported for the Brooks Range (Fig. 9). The decline in S-Ratios between 9.8 and 6.7 ka (Fig. 9), therefore cannot represent the immediate cessation of dust production from glacial abrasion. The continued alluviation of material from glacial catchments following retreat could have contributed a local source of dust to Burial Lake, which would have declined over time as source material dwindled. However, Hamilton (2009) observed that post-Itkillik basin-filling had commenced by ~12.5 ka in some valleys of the central Brooks Range – too early to fully explain the decline in S-Ratios that extends well into the mid-Holocene.

Given the gentle sloping topography of the remaining portions of the Beringian Steppe, sea level rise, on the order of 37 m between 9.8 and 6.7 ka (Fig. 9; Clark et al., 2009), corresponded to a massive reduction in land area (Fig. 10), and could very well explain the early to mid-Holocene decline in dust input at Burial Lake. Though paleo-shorelines are binned from 10 ka to present in Fig. 10, nearly all of the remaining area was inundated before ~7 ka, when sea level stabilized and Alaskan shorelines approached their present-day configurations. Intriguingly, S-Ratios stabilize around the same time (Fig. 9), hinting at a possible causal relationship. Sea level rise, however, is likely not the sole cause of dust emissions in the Holocene, given that the late Holocene increase in S-Ratios ~2 ka, occurs after sea level had already stabilized (Fig. 9).

This recent intensification of dustiness implied by increasing S-Ratios from ~2 ka is also difficult to rationalize given the available proxy evidence that indicates generally wet and warm climatic conditions for central Alaska in the last few millennia (e.g. Abbott et al., 2000; Kurek et al., 2009). Other than S-Ratios, down-core physical, geochemical, and magnetic parameters do not appear to show any substantial deviation that would indicate a sudden trend towards a more arid environment (Fig. 8). Sedimentation rates do increase towards the late Holocene (Fig. 3), but this does not appear to be linked to an increase in calculated detrital flux. Water levels at Birch Lake appear stable, at near-overflow level (Fig. 9), with sedimentary evidence suggesting a late Holocene moist phase persisting throughout the last ~5.5 ka (Abbott et al., 2000). Summer insolation and NGRIP $\delta^{18}O$ do exhibit declining trends which are in phase with S-Ratios (Fig. 9), but as the only supporting evidence for deteriorating climatic conditions in the recent past, we do not suspect they contributed much towards the suddenly dustier conditions.

Cosmogenic ^{10}Be exposure dates provided by Badding et al. (2013) demonstrate that late Holocene (Neoglacial) advances took place in the Kurupa and Antigun River valleys, which formed pre-LIA (Little Ice Age) moraine crests between 4.6 and 2.7 ka (Fig. 9). This is in agreement with previously published lichen-inferred ages (Ellis and Calkin, 1984), which confirm that glaciers in the Brooks Range experienced multiple similar Neoglacial advances (Fig. 9). It is conceivable then, that these Neoglacial advances supplied Burial Lake with local aeolian material, triggering the late Holocene increase in S-Ratios. Barclay et al. (2009) report Neoglacial advances for glaciers in southeast Alaska occurring as early as 4.5–4.0 ka, with major advances underway by 3.0 ka. They also describe the subsequent LIA advance as the largest Holocene expansion in southern Alaska, with ice-volumes sufficiently large enough to cause major glacio-isostatic depression and rebound (Larsen et al., 2005). Since the largest glaciers and ice fields of Alaska are confined to southern mountain ranges (and glaciers are more limited in the Brooks Range), we must consider them a potential far-field, glaciogenic source of dust to Burial Lake. Though we are currently unable to magnetically fingerprint such a source, it may better conform to our description of a low coercivity mineralogy (Cowan et al., 2006), than does known high coercivity material from the Brooks Range.

7. Conclusions

We extend our understanding of paleo-environmental variability across the Alaskan Arctic through a detailed study of Burial Lake sediments. This ~37,000-year record can be subdivided into three lithologic subunits based on observed physical, geochemical, and rock magnetic changes. The marked decrease in magnetic concentration observed through the deglacial transition, is partly attributed to biogenic/organic dilution as cold, windy, and dry glacial period conditions gave way to a warmer, more productive Holocene climate with increased moisture availability. The two main detrital constituents of Burial Lake sediments are mineralogically distinct and can be classified according to their rock magnetic characteristics. The low coercivity magnetic component is interpreted as magnetite-rich sediment that arrives via aeolian deposition of dust. The high coercivity component is interpreted as a local influx of detrital minerals, weathered from surrounding bedrock, and arriving via terrestrial seasonal runoff. Down-core rock magnetic variability indicates significant provenance changes, which we suspect are mainly driven by variable inputs of aeolian dust. The diminished relative contribution of the low coercivity ferrimagnetic component from the glacial period to the Holocene, along with a significant reduction in detrital flux, suggests the decrease in magnetic concentration is also largely attributed to a decrease in clastic aeolian flux.

Taking advantage of a well-constrained chronology and a simple depositional environment, we compare the timing and extent of aeolian deposition in Burial Lake with regional proxy data to constrain regional and far-field sources of dust and identify the possible forcing mechanisms that control its production, availability, transport, and deposition. The climatic amelioration associated with the deglacial transition appears to have limited landscape deflation that likely supplied Burial Lake with a widespread source of dust during the glacial period. The similarity of S-Ratios to regional lake level reconstructions suggests that dust input is regulated to a large degree by general aridity. As a result, S-Ratios can be used elsewhere in Alaska to estimate dust flux and general aridity at a much higher resolution, adding a needed dimension to ongoing paleoclimate research in Alaska.

Although the Alaskan loess is typically assumed to be glaciogenic in origin, we at times observe little correlation between dust input to Burial Lake and regional glacial activity. This suggests that regional glaciers in the Brooks Range may not be the sole, or even major, contributors of dust to Burial Lake, or that the availability of dust for transport and its timing of deposition is more broadly dependent on regional climate.

Lastly, the similarity of S-Ratios to relative sea level demonstrates the significance of newly exposed continental shelves as a potential far-field source of dust to interior Alaska. Future studies of terrestrial loess deposits should therefore consider continental shelves as a viable source of dust, which may communicate valuable long-range paleo-environmental signals.

Acknowledgments

This research was supported by the National Science Foundation under grant# NSF-ARC 0909545. We would like to thank Dr. Nathan Stansell for his help with fieldwork at Burial Lake in 2010, Jacques Labrie and Sylvain Leblanc at ISMER for their assistance with u-channel measurements and data processing, the staff at INRS-ETE for their assistance with CT scanning, Dr. Bernard Housen and Russell Burmester at Western Washington University for the use of

their facilities and rock magnetic instruments, and to our many colleagues and friends at CEOAS, particularly Dr. Alan Mix and Dr. Anders Carlson for their help and insight throughout this study. We also thank the editor, and two anonymous reviewers whose comments greatly improved this manuscript.

Appendix A. Supplementary data

Supplementary data related to this article can be found at http://dx.doi.org/10.1016/j.quascirev.2015.08.018.

References

Abbott, M.B., Edwards, M.E., Finney, B.P., 2010. A 40,000-yr record of environmental change from Burial Lake in Northwest Alaska. Quat. Res. 74, 156–165.
Abbott, M.B., Finney, B.P., Edwards, M.E., Kelts, K.R., 2000. Lake-level reconstruction and paleohydrology of Birch Lake, Central Alaska, based on seismic reflection profiles and core transects. Quat. Res. 53, 154–166.
Ager, T.A., 1975. Late Quaternary Environmental History of the Tanana Valley, Alaska. Research Foundation and the Institute of Polar Studies, The Ohio State University, Columbus, Ohio.
Anderson, N., Rippey, B., 1988. Diagenesis of magnetic minerals in the recent sediments of a eutrophic lake. Limnol. Oceanogr. 1476–1492.
Badding, M.E., Briner, J.P., Kaufman, D.S., 2013. ^{10}Be ages of late Pleistocene deglaciation and Neoglaciation in the north-central Brooks Range, Arctic Alaska. J. Quat. Sci. 28, 95–102.
Barclay, D.J., Wiles, G.C., Calkin, P.E., 2009. Holocene glacier fluctuations in Alaska. Quat. Sci. Rev. 28, 2034–2048.
Begét, J.E., 1990. Middle wisconsinan climate fluctuations recorded in Central Alaskan loess. Géogr. phys. Quaternaire 44, 3–13.
Begét, J.E., 2001. Continuous late quaternary proxy climate records from loess in Beringia. Quat. Sci. Rev. 20, 499–507.
Begét, J.E., Stone, D.B., Hawkins, D.B., 1990. Paleoclimatic forcing of magnetic susceptibility variations in Alaskan loess during the late quaternary. Geology 18, 40–43.
Berger, A., Loutre, M.F., 1991. Insolation values for the climate of the last 10 million years. Quat. Sci. Rev. 10, 297–317.
Bigelow, N.H., Begét, J., Powers, R., 1990. Latest Pleistocene increase in wind intensity recorded in eolian sediments from central Alaska. Quat. Res. 34, 160–168.
Bigelow, N.H., 1997. Late-Quaternary Climate and Vegetation in Interior Alaska. University of Alaska, Fairbanks, Fairbanks, AK.
Bigelow, N.H., Edwards, M.E., 2001. A 14,000 yr paleoenvironmental record from Windmill Lake, Central Alaska: lateglacial and holocene vegetation in the Alaska range. Quat. Sci. Rev. 20, 203–215.
Bird, B., Abbott, M., Finney, B., Kutchko, B., 2009. A 2000 year varve-based climate record from the central Brooks Range, Alaska. J. Paleolimnol. 41, 25–41.
Blaauw, M., 2010. Methods and code for "classical" age-modelling of radiocarbon sequences. Quat. Geochronol. 5, 512–518.
Blott, S.J., Pye, K., 2001. GRADISTAT: a grain size distribution and statistics package for the analysis of unconsolidated sediments. Earth Surf. Process. Landforms 26, 1237–1248.
Briner, J.P., Kaufman, D.S., 2008. Late Pleistocene mountain glaciation in Alaska: key chronologies. J. Quat. Sci. 23, 659–670.
Broecker, W.S., 1994. Massive iceberg discharges as triggers for global climate change. Nature 372, 421–424.
Canfield, D.E., Berner, R.A., 1987. Dissolution and pyritization of magnetite in anoxic marine sediments. Geochim. Cosmochim. Acta 51, 645–659.
Carlson, L.J., Finney, B.P., 2004. A 13 000-year history of vegetation and environmental change at Jan Lake, east-central Alaska. Holocene 14, 818–827.
Clark, P.U., Dyke, A.S., Shakun, J.D., Carlson, A.E., Clark, J., Wohlfarth, B., Mitrovica, J.X., Hostetler, S.W., McCabe, A.M., 2009. The last glacial maximum. Science 325, 710–714.
Clark, P.U., Shakun, J.D., Baker, P.A., Bartlein, P.J., Brewer, S., Brook, E., Carlson, A.E., Cheng, H., Kaufman, D.S., Liu, Z., Marchitto, T.M., Mix, A.C., Morrill, C., Otto-Bliesner, B.L., Pahnke, K., Russell, J.M., Whitlock, C., Adkins, J.F., Blois, J.L., Clark, J., Colman, S.M., Curry, W.B., Flower, B.P., He, F., Johnson, T.C., Lynch-Stieglitz, J., Markgraf, V., McManus, J., Mitrovica, J.X., Moreno, P.I., Williams, J.W., 2012. Global climate evolution during the last deglaciation. Proc. Natl. Acad. Sci. 109 (19), E1134–E1142.
Cowan, E.A., Brachfeld, S.A., Powell, R.D., Schoolfield, S.C., 2006. Terrane-specific rock magnetic characteristics preserved in glacimarine sediment from southern coastal Alaska. Can. J. Earth Sci. 43, 1269–1282.
Davies, M.H., Mix, A.C., Stoner, J.S., Addison, J.A., Jaeger, J., Finney, B., Wiest, J., 2011. The deglacial transition on the southeastern Alaska Margin: meltwater input, sea level rise, marine productivity, and sedimentary anoxia. Paleoceanography 26, PA2223.
Day, R., Fuller, M., Schmidt, V., 1977. Hysteresis properties of titanomagnetites: grain-size and compositional dependence. Phys. Earth Planet. Interiors 13, 260–267.
Duchesne, M.J., Moore, F., Long, B.F., Labrie, J., 2009. A rapid method for converting medical computer tomography scanner topogram attenuation scale to Hounsfield unit scale and to obtain relative density values. Eng. Geol. 103, 100–105.
Dunlop, D.J., Özdemir, Ö., 2001. Rock Magnetism: Fundamentals and Frontiers. Cambridge University Press.
Elias, S.A., Short, S.K., Birks, H.H., 1997. Late Wisconsin environments of the Bering Land Bridge. Palaeogeogr. Palaeoclimatol. Palaeoecol. 136, 293–308.
Ellersieck, I., Curtis, S.M., Mayfield, C.F., Tailleur, I.L., 1984. Reconnaissance Geologic Map of South-central Misheguk Mountain Quadrangle, Alaska: U.S. Geological Survey Miscellaneous Investigations Series Map 1504, 2 Sheets, Scale 1:63,360.
Ellis, J.M., Calkin, P.E., 1984. Chronology of holocene glaciation, central Brooks Range, Alaska. Geol. Soc. Am. Bull. 95, 897–912.
Evans, M.E., Jensen, B.J.L., Kravchinsky, V.A., Froese, D.G., 2011. The Kamikatsura event in the Gold Hill loess, Alaska. Geophys. Res. Lett. 38, L13302.
Evans, M.M.E., Heller, F.A., 2003. Environmental Magnetism: International Geophysics Series. Academic Press, Incorporated.
Finkenbinder, M.S., Abbott, M.B., Steinman, B.A., Edwards, M.E., Langdon, C.T., Finney, B.P., 2014. A 31,000 year record of paleoenvironmental and lake-level change from Harding Lake, Alaska, USA. Quat. Sci. Rev. 87, 98–113.
Finkenbinder, M.S., Abbott, M.B., Stoner, J.S., Dorfman, J.M., 2015. A multi-proxy reconstruction of environmental change spanning the last 37,000 years from Burial Lake, Arctic Alaska. Quat. Sci. Rev. (in this issue).
Fortin, D., Francus, P., Gebhardt, C., Hahn, A., Kliem, P., Labrie, J., Lise-Pronovost, A., Roychowdhury, R., St-Onge, G., Zolitschka, B., the PASADO Science Team, 2013. Density variability of the PASADO long composite record: method comparison and interpretation. Quat. Sci. Rev. 71, 147–153.
Frank, U., Nowaczyk, N.R., 2008. Mineral magnetic properties of artificial samples systematically mixed from haematite and magnetite. Geophys. J. Int. 175, 449–461.
Hamilton, T.D., 1982. A late Pleistocene glacial chronology for the southern Brooks Range: stratigraphic record and regional significance. Geol. Soc. Am. Bull. 93, 700–716.
Hamilton, T.D., 2001. Quaternary glacial, lacustrine, and fluvial interactions in the western Noatak basin, Northwest Alaska. Quat. Sci. Rev. 20, 371–391.
Hamilton, T.D., 2003. Surficial Geology of the Dalton Highway (Itkillik-sagavanirktok Rivers) Area, Southern Arctic Foothills, Alaska. Alaska Dept. of Natural Resources, Division of Geological and Geophysical Surveys, Fairbanks, Alaska.
Hamilton, T.D., 2009. Guide to Surficial Geology and River-bluff Exposures, Noatak National Preserve, Northwestern Alaska. U.S. Geological Survey Scientific Investigations Report 2008-5125, p. 116. http://pubs.usgs.gov/sir/2008/5125/.
Hamilton, T.D., 2010. Surficial Geologic Map of the Noatak National Preserve, Alaska: U.S. Geological Survey Scientific Investigations Map 3036, 1 Sheet, Scale 1:250, 000, 1 Pamphlet, p. 21.
Hamilton, T.D., Labay, K.A., 2011. Surficial Geologic Map of the Gates of the Arctic National Park and Preserve, Alaska: U.S. Geological Survey Scientific Investigations Map 3125, Pamphlet 19 p., Scale 1:300,000. Available from: http://pubs.usgs.gov/sim/3125/.
Hamilton, T.D., Van Etten, D.P., 1984. Late Pleistocene glacial dams in the Noatak valley. In: Coonrad, W.L., Elliott, R.L. (Eds.), The United States Geological Survey in Alaska: Accomplishments During 1981. U.S. Geol. Survey Circular 868, pp. 21–23.
Hatfield, R.G., Stoner, J.S., 2013. Magnetic proxies and susceptibility. In: Elias, S.A. (Ed.), The Encyclopedia of Quaternary Science, vol. 2. Elsevier, Amsterdam, pp. 884–898.
Heslop, D., Dekkers, M.J., Kruiver, P.P., Van Oorschot, I.H.M., 2002. Analysis of isothermal remanent magnetization acquisition curves using the expectation–maximization algorithm. Geophys. J. Int. 148, 58–64.
Hopkins, D.M., 1982. Aspects of the Paleogeography of Beringia during the Late Pleistocene. Paleoecology of Beringia. Academic Press, New York, pp. 3–28.
Hostetler, S.W., Clark, P.U., Bartlein, P.J., Mix, A.C., Pisias, N.J., 1999. Atmospheric transmission of North Atlantic Heinrich events. J. Geophys. Res. 104, 3947–3952.
Hounsfield, G.N., 1973. Computerized transverse axial scanning (tomography): I. description of system. Br. J. Radiol. 46 (552), 1016–1022.
Hutchins, D.A., Bruland, K.W., 1998. Iron-limited diatom growth and Si:N uptake ratios in a coastal upwelling regime. Nature 393, 561–564.
Huybers, P., Wunsch, C., 2004. A depth-derived Pleistocene age model: uncertainty estimates, sedimentation variability, and nonlinear climate change. Paleoceanography 19, PA1028.
Imbrie, J., 1963. Factor and vector analysis programs for analyzing geologic data. Tech. Rep. 6, Geogr. Branch, Off. of Nav. Res. Washington, D.C.
Karlin, R., Levi, S., 1983. Diagenesis of magnetic minerals in recent hemipelagic sediments. Nature 303, 327–330.
King, J.W., Channel, J.E.T., 1991. Sedimentary magnetism, environmental magnetism, and magnetostratigraphy. Rev. Geophys. (Supplement), 358–370.
Kohfeld, K.E., Harrison, S.P., 2001. DIRTMAP: the geological record of dust. Earth Sci. Rev. 54, 81–114.
Kurek, J., Cwynar, L.C., Ager, T.A., Abbott, M.B., Edwards, M.E., 2009. Late quaternary paleoclimate of western Alaska inferred from fossil chironomids and its relation to vegetation histories. Quat. Sci. Rev. 28, 799–811.
Lagroix, F., Banerjee, S.K., 2002. Paleowind directions from the magnetic fabric of loess profiles in central Alaska. Earth Planet. Sci. Lett. 195, 99–112.
Larsen, C.F., Motyka, R.J., Freymueller, J.T., Echelmeyer, K.A., Ivins, E.R., 2005. Rapid viscoelastic uplift in southeast Alaska caused by post-little Ice Age glacial retreat. Earth Planet. Sci. Lett. 237, 548–560.
Liu, X.M., Hesse, P., Rolph, T., Begét, J.E., 1999. Properties of magnetic mineralogy of

Alaskan loess: evidence for pedogenesis. Quat. Int. 62, 93–102.
Mann, D.H., Peteet, D.M., Reanier, R.E., Kunz, M.L., 2002. Responses of an arctic landscape to lateglacial and early Holocene climate changes: the importance of moisture. Quat. Sci. Rev. 21, 997–1021.
Marcott, S.A., Shakun, J.D., Clark, P.U., Mix, A.C., 2013. A reconstruction of regional and global temperature for the past 11,300 years. Science 339, 1198–1201.
Mayfield, C.F., Curtis, S.M., Ellersieck, I., Tailleur, I.L., 1984. Reconnaissance Geologic Map of Southeastern Misheguk Mountain Quadrangle, Alaska: U.S. Geological Survey Miscellaneous Investigations Series Map 1503, 2 Sheets, Scale 1:63,360.
Milne, G.A., Mitrovica, J.X., 2008. Searching for eustasy in deglacial sea-level histories. Quat. Sci. Rev. 27, 2292–2302.
Mikolajewicz, U., Crowley, T.J., Schiller, A., Voss, R., 1997. Modelling teleconnections between the North Atlantic and North Pacific during the Younger Dryas. Nature 387, 384–387.
Muhs, D.R., Ager, T.A., Arthur Bettis III, E., McGeehin, J., Been, J.M., Begét, J.E., Pavich, M.J., Stafford Jr., T.W., Stevens, D.A.S.P., 2003a. Stratigraphy and palaeoclimatic significance of late quaternary loess–palaeosol sequences of the last interglacial–glacial cycle in central Alaska. Quat. Sci. Rev. 22, 1947–1986.
Muhs, D.R., Ager, T.A., Been, J., Bradbury, J.P., Dean, W.E., July 2003b. A late quaternary record of eolian silt deposition in a maar lake, St. Michael Island, western Alaska. Quat. Res. 60, 110–122.
Muhs, D.R., Budahn, J.R., 2006. Geochemical evidence for the origin of late quaternary loess in central Alaska. Can. J. Earth Sci. 43, 323–337.
North Greenland Ice Core Project Members, 2004. High-resolution record of Northern Hemisphere climate extending into the last interglacial period. Nature 431, 147–151.
Oswald, W.W., Anderson, P.M., Brown, T.A., Brubaker, L.B., Feng Sheng, Hu, Lozhkin, A.V., Tinner, W., Kaltenrieder, P., 2005. Effects of sample mass and macrofossil type on radiocarbon dating of arctic and boreal lake sediments. Holocene 15, 758–767.
Péwé, T.L., 1955. Origins of the upland silt near Fairbanks, Alaska. Geol. Soc. Am. Bull. 66, 699–724.
Praetorius, S.K., Mix, A.C., 2014. Synchronization of North Pacific and Greenland climates preceded abrupt deglacial warming. Science 345, 444–448.
Rasmussen, S.O., Andersen, K.K., Svensson, A.M., Steffensen, J.P., Vinther, B.M., Clausen, H.B., Siggaard-Andersen, M.-L., Johnsen, S.J., Larsen, L.B., Dahl-Jensen, D., Bigler, M., Röthlisberger, R., Fischer, H., Goto-Azuma, K., Hansson, M.E., Ruth, U., 2006. A new Greenland ice core chronology for the last glacial termination. J. Geophys. Res. 111, D06102.
Rea, D.K., 1994. The paleoclimatic record provided by eolian deposition in the deep sea: the geologic history of wind. Rev. Geophys. 32, 159–195.
Reimer, P.J., Baillie, M.G.L., Bard, E., Bayliss, A., Beck, J.W., Blackwell, P.G., Ramsey, C.B., Buck, C.E., Burr, G.S., Edwards, R.L., Friedrich, M., Grootes, P.M., Guilderson, T.P., Hajdas, I., Heaton, T.J., Hogg, A.G., Hughen, K.A., Kaiser, K.F., Kromer, B., McCormac, F.G., Manning, S.W., Reimer, R.W., Richards, D.A., Southon, J.R., Talamo, S., Turney, C.S.M., Plicht, J. van der, Weyhenmeyer, C.E., 2009. IntCal09 and Marine09 radiocarbon age calibration curves, 0–50,000 years cal BP. Radiocarbon 51, 1111–1150.
Rowan, C.J., et al., 2009. Reductive diagenesis, magnetite dissolution, greigite growth and paleomagnetic smoothing in marine sediments: a new view. EPSL 227, 223–235.
Ryan, W.B.F., Carbotte, S.M., Coplan, J.O., O'Hara, S., Melkonian, A., Arko, R., Weissel, R.A., Ferrini, V., Goodwillie, A., Nitsche, F., Boncz-kowski, J., Zemsky, R., 2009. Global multi-resolution topography synthesis. Geochem. Geophys. Geosyst. 10, Q03014. http://dx.doi.org/10.1029/2008GC002332.
Slack, J.F., Dumoulin, J.A., Schmidt, J.M., Young, L.E., Rombach, C.S., 2004. Paleozoic sedimentary rocks in the red dog Zn-Pb-Ag district and vicinity, Western Brooks Range, Alaska: provenance, deposition, and metallogenic significance. Econ. Geol. 99, 1385–1414.
Snowball, I.F., 1993. Geochemical control of magnetite dissolution in sub-arctic lake sediments and the implications for environmental magnetism. J. Quat. Sci. 8, 339–346.
St-Onge, G., Stoner, J.S., Hillaire-Marcel, C., 2003. Holocene paleomagnetic records from the St. Lawrence Estuary, eastern Canada: centennial- to millennial-scale geomagnetic modulation of cosmogenic isotopes. Earth Planet. Sci. Lett. 209, 113–130.
Stober, J.C., Thompson, R., 1979. An investigation into the source of magnetic minerals in some Finnish lake sediments. Earth Planet. Sci. Lett. 45, 464–474.
Stoner, J.S., St-Onge, G., 2007. Chapter three magnetic stratigraphy in paleoceanography: reversals, excursions, paleointensity, and secular variation. Dev. Mar. Geol. 1, 99–138.
Stuiver, M., Reimer, P.J., Reimer, R.W., 2005. CALIB 5.0 [program and documentation]. http://calib.qub.ac.uk/calib/.
Tauxe, L., 1993. Sedimentary records of relative paleointensity of the geomagnetic field: theory and practice. Rev. Geophys. 31, 319–354.
Tegen, I., Lacis, A.A., Fung, I., 1996. The influence on climate forcing of mineral aerosols from disturbed soils. Nature 380, 419–422.
Thompson, R., Oldfield, F., 1986. Environmental Magnetism. Allen & Unwin.
Vlag, P.A., Oches, E.A., Banerjee, S.K., Solheid, P.A., 1999. The paleoenvironmental-magnetic record of the Gold Hill Steps loess section in central Alaska. Phys. Chem. Earth Part A Solid Earth Geodesy 24, 779–783.
Xuan, C., Channell, J.E.T., 2009. UPmag: MATLAB software for viewing and processing u channel or other pass-through paleomagnetic data. Geochem. Geophys. Geosyst. 10, Q10Y07.